



Development of the tangent linear and adjoint models of the global online chemical transport model MPAS-CO₂ v7.3

Tao Zheng^{1,7}, Sha Feng², Jeffrey Steward³, Xiaoxu Tian⁴, David Baker⁵, and Martin Baxter⁶

¹Department of Geography and Environmental Studies, Central Michigan University, Mount Pleasant, MI. USA

²Atmospheric Sciences and Global Change Division, Pacific Northwest National Laboratory, Richland, WA. USA

³Data Assimilation Intelligence for Space Systems, LLC., Boulder, CO. USA

⁴Tomorrow.io, Boston, MA. USA

⁵Cooperative Institute for Research in the Atmosphere, Colorado State University, Fort Collins, CO. USA

⁶Department of Earth and Atmospheric Science, Central Michigan University, Mount Pleasant, MI. 48858

⁷Institute for Great Lakes Research, Central Michigan University, Mount Pleasant, MI. USA

Correspondence: Tao Zheng(zheng1t@cmich.edu)

Abstract. We describe the development of the tangent linear (TL) and adjoint models of the MPAS-CO₂ transport model, which is a global online chemical transport model developed upon the non-hydrostatic Model for Prediction Across Scales-Atmosphere (MPAS-A). The primary goal is to make the model system a valuable research tool for investigating atmospheric carbon transport and inverse modeling. First, we develop the TL code, encompassing all CO₂ transport processes within the MPAS-CO₂ forward model. Then, we construct the adjoint model using a combined strategy involving re-calculation and storage of the essential meteorological variables needed for CO₂ transport. This strategy allows the adjoint model to undertake long-period integration with moderate memory demands. To ensure accuracy, the TL and adjoint models undergo vigorous verifications through a series of standard tests. The adjoint model, through backward-in-time integration, calculates the sensitivity of atmospheric CO₂ observations to surface CO₂ fluxes and the initial atmospheric CO₂ mixing ratio. To demonstrate the utility of the newly-developed adjoint model, we conduct simulations for two types of atmospheric CO₂ observations: tower-based *in situ* CO₂ mixing ratio and satellite-derived column-averaged (X_{CO_2}). A comparison between the sensitivity to surface flux calculated by the MPAS-CO₂ adjoint model with its counterpart from Carbon Tracker-Lagrange (CT-L) reveals spatial agreement but notable magnitude differences. These differences, particularly evident for X_{CO_2} , likely arise from differences in vertical mixing between the two systems. Moreover, this comparison highlights the substantial loss of information in the atmospheric CO₂ observations due to CT-L's simulation length and spatial domain limitations. Furthermore, the adjoint sensitivity analysis demonstrates that the sensitivities to both surface flux and initial CO₂ conditions spread out throughout the entire northern hemisphere within a month. MPAS-CO₂ forward, TL, and adjoint models stand out for their calculation efficiency and variable-resolution capability, making them competitive in computational cost. In conclusion, the successful development of the MPAS-CO₂ TL and adjoint models, and their integration into the MPAS-CO₂ system, establish the possibility of using MPAS's unique features in atmospheric CO₂ transport sensitivity studies and in inverse modeling with advanced methods such as variational data assimilation.



1 Introduction

Estimating CO₂ fluxes through inverse modeling, using atmospheric chemical transport models and atmospheric CO₂ measurements, is an important approach for understanding the global carbon budget. Beyond providing seasonal flux estimates that are useful for understanding the magnitude and phase of photosynthesis and respiration, it provides annual mean flux estimates that shed light on the key processes driving the response to climate change. When these annual mean CO₂ estimates are adjusted to account for lateral fluxes (e.g., due to rivers, or the transport of crops and wood products), it gives an independent means of validating carbon stock change estimates from the terrestrial biogeochemical models and inventories (Byrne et al., 2023). However, atmospheric transport models, which play a key role in inverse modeling, remain a significant source of uncertainty on both regional and global scales (Hurtt et al., 2022).

Two classes of chemical transport models – online and offline – are commonly used for simulating atmospheric CO₂ transport. Offline models, such as TM5 (Krol et al., 2005; Meirink et al., 2006), PCTM (Kawa et al., 2004; Baker et al., 2006) and GEOS-Chem (Kopacz et al., 2009), solve the tracer continuity equation using winds and vertical mixing fields computed from an independent run of a meteorological model or from a meteorological analysis. Online models, such as WRF-Chem (Grell et al., 2011), OLAM (Walko and Avissar, 2008; Schuh et al., 2021), and MPAS-CO₂ (Skamarock et al., 2012; Zheng et al., 2021), integrate chemistry, transport and meteorology simultaneously. Although offline models typically have lower computational costs, the separation of chemistry/transport from meteorology leads to a loss of information regarding atmospheric processes occurring at time scales shorter than the meteorological model output frequency (Grell et al., 2005). In comparison, online models, owing to their simultaneous integration of meteorology and chemistry, have the potential to improve transport accuracy, particularly for vertical transport of chemistry. Recent advances in computer power and parallelization have greatly reduced the computational cost of online transport models, making them increasingly more accessible and practical for atmospheric CO₂ research.

A number of studies have demonstrated that transport model accuracy can be improved by increasing the model's horizontal resolution (Feng et al., 2016; Agusti-Panareda et al., 2019). Because global high-resolution CO₂ transport simulations are computationally demanding, limited-area models (regional models) are often used instead (Pillai et al., 2012; Lauvaux et al., 2012; Zheng et al., 2018). However, regional models introduce the lateral boundary condition, posing challenges for CO₂ inverse modeling (Zheng et al., 2019; Rayner et al., 2019). MPAS-CO₂ (Zheng et al., 2021) addresses this limitation by being an online global transport model based on the compressible non-hydrostatic Model for Prediction Across Scales-Atmosphere (MPAS-A) (Skamarock et al., 2012). Like OLAM (Schuh et al., 2021), MPAS-CO₂ uses a global variable-resolution mesh to facilitate local grid refinement for high-resolution simulations in specific regions without incurring prohibitively high computational costs and avoiding the disadvantages of lateral boundary conditions.



55 The primary objective of this study is to develop the tangent linear (TL) and adjoint (AD) models associated with the global online transport model MPAS-CO₂ (Zheng et al., 2021). Adjoint model techniques have been widely used in both meteorological and atmospheric greenhouse gas research (Errico, 1997; Courtier et al., 1994; Giering et al., 2006; Meirink et al., 2008; Henze et al., 2007; Tian and Zou, 2021), and play critical roles in variational data assimilation and sensitivity analyses (Baker et al., 2006; Zheng et al., 2018; Tian and Zou, 2020).

60

The subsequent sections of this paper provide an overview of the MPAS-CO₂ forward model developed in Zheng et al. (2021) (Section 2), and the development and verification of the TL and AD models based on the forward model (Sections 3 & 4). The utility of the newly developed AD model is demonstrated with adjoint sensitivity analyses in Section 5. Finally, a summary and conclusion are given in Section 6.

65 2 MPAS-CO₂ forward model

Zheng et al. (2021) documented the development of MPAS-CO₂, verifying its mass conservation and assessing its accuracy. Hereafter, we refer to MPAS-CO₂ as the forward model, whose TL and AD model counterparts we develop in the present paper. A brief description of the forward model is provided here; see Zheng et al. (2021) for comprehensive details. The forward model characterizes CO₂ transport through the continuity equation:

$$70 \quad \frac{\partial(\tilde{\rho}q_{co_2})}{\partial t} = -(\nabla \cdot \tilde{\rho}q_{co_2} \mathbf{V})_{\zeta} + F_{bl} + F_{cu} \quad (1)$$

where q_{co_2} is CO₂ dry air mixing ratio, $\tilde{\rho} = \rho_d / (\partial\zeta/\partial z)$, ρ_d is dry air density, ζ is the vertical coordinate, z is geometric height, t is time, and $\mathbf{V} = (u, v, w)$ is the velocity vector (u , v , and w are the zonal, meridional, and vertical wind components, respectively). The meteorological variables, such as wind velocity and dry air density, are updated simultaneously with CO₂ by the model's dynamical core and physics parameterizations. The left-hand side (LHS) of Eq. (1) is the total CO₂ time tendency
 75 $(\partial(\tilde{\rho}q_{co_2})/\partial t)$, and the first, second, and third terms on the right-hand side (RHS) represent the contributions from advection, vertical mixing by the planetary boundary layer (PBL) parameterization, and convective transport, respectively. Advection of CO₂ in MPAS-CO₂ is handled in the model's dynamical core and can be expressed as Eq. (2), where the first two terms on the RHS represent the horizontal advection, and the third term represents the vertical advection:

$$(\nabla \cdot \tilde{\rho}q_{co_2} \mathbf{V})_{\zeta} = \left[\frac{\partial(\tilde{\rho}uq_{co_2})}{\partial x} + \frac{\partial(\tilde{\rho}vq_{co_2})}{\partial y} \right]_{\zeta} + \frac{\partial(\tilde{\rho}wq_{co_2})}{\partial \zeta} \quad (2)$$

80 CO₂ vertical mixing in the PBL is implemented based on the YSU PBL scheme (Hong et al., 2006) and can be expressed as:

$$F_{bl} = \frac{\partial q_{co_2}}{\partial t} = \frac{\partial}{\partial z} \left[K_h \left(\frac{\partial q_{co_2}}{\partial z} \right) - \overline{(w'q'_{co_2})}_h \left(\frac{z}{h} \right)^3 \right] \quad (3)$$



where z is the vertical distance to surface, h is boundary layer top height, and K_h is vertical eddy diffusivity. Convective transport of CO_2 is implemented based on the Kain-Fristch convection scheme (Kain, 2004) and it can be expressed as Eq. (4)

$$85 \quad F_{cu} = \frac{\partial q_{\text{CO}_2}}{\partial t} = \frac{(M_u + M_d)}{\rho A} \frac{\partial q_{\text{CO}_2}}{\partial z} + \frac{M_{ud}}{M} (q_{\text{CO}_2}^u - q_{\text{CO}_2}) + \frac{M_{dd}}{M} (q_{\text{CO}_2}^d - q_{\text{CO}_2}) \quad (4)$$

where q_{CO_2} , $q_{\text{CO}_2}^u$, and $q_{\text{CO}_2}^d$ are the CO_2 mixing ratio in the environment, updraft, and downdraft, respectively, M_u and M_d are the updraft and downdraft mass, respectively, ρ is the environment air density, A is the horizontal area of a cell, $M = \rho A \delta z$ is the mass of environmental air in a grid box, and M_{ud} and M_{dd} are the detrainment from the updraft and downdraft, respectively.

90 3 Development of the MPAS- CO_2 TL model

The CO_2 advective transport process described in Eq. (2) is implemented by two two different numerical schemes in the forward model: (1) a monotonic scheme with hyperviscosity (β) set to 0.25; and (2) a non-monotonic scheme with $\beta = 1.0$ (Skamarock et al., 2012). The monotonicity in the first scheme is achieved by applying a flux limiter in the last step of the third-order Runge-Kutta solver (Wang et al., 2009; Skamarock and Gassmann, 2011). While the second scheme is linear in
95 CO_2 , the first scheme is nonlinear due to the application of the flux limiter. Because both the YSU PBL and Kain-Fristch convection schemes are linear in CO_2 , using the linear advective scheme makes the forward model a linear model in CO_2 . In this paper, we develop the TL and adjoint models based on the linear version of the MPAS- CO_2 forward model, which can be symbolically expressed as:

$$\mathbf{x}_t = \mathcal{M}(\mathbf{x}_0, \mathbf{e}), \quad (5)$$

100 where \mathbf{x}_0 and \mathbf{x}_t are the CO_2 dry air mixing ratio at the initial and forecast time (t), respectively. $\mathcal{M}(\cdot)$ represents the MPAS- CO_2 forward model and \mathbf{e} represents a timeseries of CO_2 fluxes between times 0 and t . While both \mathbf{x}_0 and \mathbf{x}_t are 3-dimensional vectors, \mathbf{e} is 2-dimensional, indicating that CO_2 flux is applied only to the model's surface cells. Eq.(5) indicates that CO_2 mixing ratio at a forecast time (\mathbf{x}_t) is determined by the CO_2 mixing ratio at an initial time (\mathbf{x}_0) and the CO_2 flux (\mathbf{e}) through the forward model.

105

The TL and adjoint models are designed to calculate the sensitivity of \mathbf{X}_t with respect to \mathbf{x}_0 and \mathbf{e} . This is achieved by introducing the TL and adjoint variables of their counterparts in the forward model (Giles and Pierce, 2000). While the introduction of the TL and adjoint variables for the initial CO_2 mixing ratio (\mathbf{x}_0) is straightforward, it is a bit more complex for the CO_2 fluxes (\mathbf{e}). This complexity arises from the fact that CO_2 flux, at each surface cell of the model, varies with time
110 throughout the model's entire simulation period. Depending on the underlying biosphere model and emission inventory used, CO_2 flux varies at a certain temporal frequency, ranging from hourly to monthly. Although it is possible to introduce TL and



adjoint variables for CO₂ flux at the flux's temporal frequency, it is neither practical nor necessary to do so. Instead, a common approach is to introduce flux scaling factors (Henze et al., 2007; Zheng et al., 2018) as follows:

$$\mathbf{e} = \mathbf{S}(\mathbf{k})\tilde{\mathbf{e}}, \quad (6)$$

115 where $\tilde{\mathbf{e}}$ are time-variant CO₂ fluxes, typically from a process model or inventory, and $\mathbf{S}(\mathbf{k})$ is a generic scaling function. Eq. (6) means that at each surface cell, the magnitude of the CO₂ flux ($\tilde{\mathbf{e}}$) is adjusted using a flux scaling factor before it is used to modify the cell's CO₂ mixing ratio. We implemented Eq. (6) in an emission driver of the forward model in a way that allows the flexibility of choosing the temporal frequency of the flux scaling factor. For instance, for a 24-hour forward model simulation forced by 3-hourly CO₂ flux, one can choose to have eight scaling factors at each surface cell (one for each of
120 the eight 3-hour segments), or just one scaling factor for the entire time period. All the MPAS-CO₂ model runs used in the remainder of this paper are conducted using a single scaling factor for each surface cell that is repeated for each flux timestep in the entire simulation period. In this case, the scaling function $\mathbf{S}(\mathbf{k})$ in Eq. (6) is a function of a scaling vector \mathbf{k} that has the same dimension as the model's surface mesh. The introduction of the flux scaling factors turns CO₂ flux from active variables to parameters, and the impacts of their variation on CO₂ mixing ratio are calculated through their corresponding scaling factors
125 \mathbf{k} . Accordingly, the MPAS-CO₂ forward model can be symbolically expressed as

$$\mathbf{x}_t = \mathcal{M}(\mathbf{x}_0, \mathbf{k}) \quad (7)$$

Eq. (7) shows that for a given set of CO₂ flux ($\tilde{\mathbf{e}}$), the forecast time CO₂ mixing ratio (\mathbf{x}_t) is a function of the initial time CO₂ mixing ratio (\mathbf{x}_0) and the flux scaling factor (\mathbf{k}).

130 The TL counterpart of the MPAS-CO₂ forward model represented by Eq. (7) can be symbolically expressed as the first derivative of the forward model:

$$\Delta \mathbf{x}_t = \mathbf{M}(\Delta \mathbf{x}_0, \Delta \mathbf{k}) \quad (8)$$

where $\mathbf{M}(\)$ represents the MPAS-CO₂ TL model, $\Delta \mathbf{x}_0$ and $\Delta \mathbf{x}_t$ are the TL variable of CO₂ mixing ratio at the initial and forecast time, respectively, and $\Delta \mathbf{k}$ is the TL variable of the flux scaling factor \mathbf{k} . In essence, Eq. (8) shows that the TL model
135 computes the perturbation in the forecast time CO₂ mixing ratio ($\Delta \mathbf{x}_t$), given the perturbation in the flux scaling factor ($\Delta \mathbf{k}$) and/or perturbation in the initial time CO₂ mixing ratio ($\Delta \mathbf{x}_0$).

Based on the source code of the forward model, we developed the TL code by differentiating each process relevant to CO₂ flux and transport, including advection, vertical mixing by the YSU PBL scheme, convective transport by the Kain-Fritsch
140 scheme, and the CO₂ emission driver that implements Eq. (6). Automatic differentiation tools, such as Tapenade (Hascoet and Pascual, 2013) and Tangent and Adjoint Model Compiler (Giering and Kaminski, 1998), can be used to assist TL and adjoint



code generation. However, the code these tools generate typically contains redundancies and is difficult to read, particularly for the adjoint code. To optimize the computation efficiency and facilitate future code upgrading, we manually developed the TL and adjoint code for MPAS-CO₂ with some minor assistance from Tapenade.

145

After the TL model is completed, a thorough examination of its correctness was undertaken. As indicated in Eq. (8), the TL model can calculate the sensitivity of \mathbf{x}_t with respect to both \mathbf{x}_0 and \mathbf{k} . The calculation of the sensitivity of \mathbf{x}_t with respect to \mathbf{x}_0 involves the TL code of all the CO₂ transport processes, including advection, PBL, and convective transport. In comparison, the calculation of the sensitivity of \mathbf{x}_t with respect to the flux scaling factor \mathbf{k} involves the TL code of the CO₂ emission driver in addition to the TL code of all the CO₂ transport processes. Because the calculation of sensitivity to \mathbf{k} includes the TL code of all the processes in the TL model, and because both the transport processes and emission driver are linear, the correctness of the entire MPAS-CO₂ TL model can be verified by checking whether the following equation is satisfied (Errico, 1997; Tian and Zou, 2020):

$$\Phi(\alpha) = \frac{\|\mathcal{M}(\mathbf{x}_0, (1 + \alpha)\mathbf{k}) - \mathcal{M}(\mathbf{x}_0, \mathbf{k})\|}{\|\mathbf{M}(0, \alpha\mathbf{k})\|} = 1, \quad (9)$$

155 where $\mathbf{M}()$ is the TL model, $\mathcal{M}()$ is the forward model and α is a scalar. The second item in the numerator of Eq. (9), $\mathcal{M}(\mathbf{x}_0, \mathbf{k})$, is a forward model run. The first item in the numerator, $\mathcal{M}(\mathbf{x}_0, (1 + \alpha)\mathbf{k})$ is an identical forward model run except that its flux scaling factor at each surface cell is adjusted by multiplying $1 + \alpha$. In the denominator, $\mathbf{M}(0, \alpha\mathbf{k})$ is a TL model run with its perturbation in initial time CO₂ mixing ratio set to zero ($\Delta\mathbf{x}_0 = 0$) and perturbation in flux scaling factor $\Delta\mathbf{k} = \alpha\mathbf{k}$, which is the difference in the flux scaling factors between the two forward model runs.

160

If the TL model is correctly coded with regard to the forward model, Eq. (9) should be satisfied to the extent of machine accuracy until α is too small that the result is affected by round-off errors and drifts away from unity. To verify using Eq. (9), we ran a series of simulations using the forward model and newly developed tangent linear model with the scale factor α ranging from 1.0×10^3 to 1.0×10^{-4} (Table 1). All the simulations start at 2018-10-01 00:00 UTC, run for 1 month, and end at 2018-11-01 00:00 UTC. The meteorological initial condition is from the ERA5 reanalysis (Hoffmann et al., 2019) and the CO₂ initial condition (\mathbf{x}_0) is from the Carbon Tracker (Jacobson et al., 2020) v2022 (CT2022) posterior CO₂ mole fraction at this time. Three-hourly CO₂ fluxes for the biogenic, fire, fossil fuel, and oceanic components from the CT2022 posterior are applied throughout the 1-month simulation period for each model run. Flux scaling factors of $\mathbf{k} = \mathbf{1}$ were used in all our simulations here, with $\mathbf{1}$ being a vector the same length as \mathbf{k} with ones in every element. The model simulations are conducted using the global variable-resolution (VR) mesh shown in Fig. 1. This VR mesh has a total of 15,898 cells, which range from 120 km over most of the land regions to 480 km over oceans. Table 1 shows that the magnitudes of both the numerator and the denominator in (9) decrease as α decreases. Moreover, the table also shows that the ratio remains close to unity until α decreases to 1.0×10^{-1} , beyond which round-off errors lead to a deviation from unity. These results confirm that the MPAS-CO₂ TL model has been correctly developed with regard to the forward model. In the next section, we proceed to develop the

170



175 MPAS-CO₂ adjoint model.

4 Development of the MPAS-CO₂ adjoint model

An adjoint model is an essential component of a variational data assimilation system and is very useful for adjoint sensitivity analysis. Symbolically, the MPAS-CO₂ adjoint model can be expressed as:

$$180 \quad (\Delta\hat{\mathbf{x}}_0, \Delta\hat{\mathbf{k}}) = \mathbf{M}^T(\Delta\hat{\mathbf{x}}_t), \quad (10)$$

where $\mathbf{M}^T(\cdot)$ is the MPAS-CO₂ adjoint model, $\Delta\hat{\mathbf{k}}$ is the adjoint variable of the flux scaling factor, and $\Delta\hat{\mathbf{x}}_0$ and $\Delta\hat{\mathbf{x}}_t$ are the adjoint variables of CO₂ mixing ratio at the initial and forecast time, respectively. Eq. (10) demonstrates that starting with $\Delta\hat{\mathbf{x}}_t$ at the forecast time, the MPAS-CO₂ adjoint model runs backward in time to the initial time, resulting in the adjoint variable of CO₂ mixing ratio at the initial time ($\Delta\hat{\mathbf{x}}_0$), and the adjoint variable of the flux scaling factor ($\Delta\hat{\mathbf{k}}$).

185

Similar to its TL model counterpart, the development of the MPAS-CO₂ adjoint model was carried out through manual implementation to avoid redundancy and optimize computational efficiency. However, unlike the forward and TL models, the adjoint model faces the challenge of accessing meteorological fields at every time step during its model integration. This challenge arises due to the fact the adjoint model runs backward in time, making the meteorological fields unavailable. One approach to this problem is saving meteorological fields in memory during the adjoint model's forward sweep, enabling access-
190 ing during the subsequent backward sweep (Guerrette and Henze, 2015; Zheng et al., 2018). However, since the MPAS-CO₂ adjoint model is intended for long simulations, this approach becomes impractical due to the excessive memory it demands. As an alternative strategy, we adopt an approach that combines both recalculation and storage of the meteorological fields. This strategy effectively divides a long simulation into segments, and the forward and backward sweeps are carried out sequentially
195 for each segment, requiring internal memory only large enough to accommodate one segment's worth of meteorological fields. This internal manipulation is handled seamlessly by the adjoint model, enabling it to run as long as needed without overburdening memory resources.

The correctness of the newly developed MPAS-CO₂ adjoint model can be verified using the following equation (Tian and
200 Zou, 2020):

$$\langle \Delta\mathbf{x}, \mathbf{M}(0, \Delta\mathbf{k}) \rangle = \langle \mathbf{M}^T(\Delta\mathbf{x}), \Delta\mathbf{k} \rangle, \quad (11)$$

where $\langle \cdot \rangle$ represents the inner product operator, $\Delta\mathbf{x}$ is a perturbation of CO₂ mixing ratio and $\Delta\mathbf{k}$ is a perturbation of CO₂ flux scaling factor. If the adjoint model is correctly coded with respect to the TL model, Eq. (11) should be satisfied for any choice of $\Delta\mathbf{x}$ and $\Delta\mathbf{k}$. $\mathbf{M}(0, \Delta\mathbf{k})$ on the LHS of the equation is the perturbation in forecast CO₂ mixing ratio resulting from



205 a TL model run whose perturbation in initial CO_2 mixing ratio is set to zero and perturbation to flux scaling factor is set to $\Delta\mathbf{k}$. The first item of the RHS, $\mathbf{M}^T(\Delta\mathbf{x})$, represents the adjoint variable of flux scaling factor output from the adjoint model integration from forecast time backward to the initial time. The TL and adjoint model runs on the two sides of Eq. (11) have the same simulation time period, but the latter runs backward in time.

210 We conducted two sets of experiments using the TL and adjoint models following Eq. (11) to verify the correctness of the newly developed adjoint model. In the first set of experiments, we set $\Delta\mathbf{k} = 10^{-1}\mathbf{1}$, and $\Delta\mathbf{x} = \mathbf{M}(0, \Delta\mathbf{k})$. The experiments were carried out in two steps: First, the TL model was integrated 7 days from the initial time (2018-10-01 00:00 UTC) to the end time (2018-10-08 00:00 UTC), with $\Delta\mathbf{k} = 10^{-1}\mathbf{1}$, resulting in $\mathbf{M}(0, \Delta\mathbf{k})$ which is the perturbation in forecast time CO_2 mixing ratio; Second, the adjoint model is initialized at 2018-10-08 00:00 UTC with its adjoint variable for CO_2 mixing
215 set to $\mathbf{M}(0, \Delta\mathbf{k})$. The adjoint model is then integrated backward in time for 7 days to 2018-10-01 00:00 UTC, resulting in $\mathbf{M}^T(\Delta\mathbf{x})$. The LHS and RHS of Eq. (11) are then calculated using the above results (Table 2). The table shows that the agreement between the LHS and RHS of Eq. (11) is about -5.15×10^{-15} . This experiment is repeated with the same configuration but the simulation length is increased to 31 days, ending at 2018-11-01 00:00 UTC. As expected, the magnitude of both the LHS and RHS increased, and they agree to about -2.55×10^{-16} . In the second set of the experiment, $\Delta\mathbf{k} = 10^{-1}\mathbf{1}$ (same as
220 the first set of experiments), but $\Delta\mathbf{x} = \mathcal{M}_{14d}(\mathbf{x}_0, \mathbf{k})$, which is the CO_2 mixing ratio at the end of 14-day forward model run (2018-10-01 00:00 UTC to 2018-10-15 00:00 UTC). We note that this forward model run uses \mathbf{x}_0 from CT2022 posterior CO_2 mole fraction, and $\mathbf{k} = \mathbf{1}$, however, Eq. (9) should satisfy for any configurations and simulation period of the forward model. The resulting LHS and RHS of Eq. (11) from the second set of experiments are about 2 orders of magnitude larger than their counterpart of the first experiments. This is caused by the much larger $\Delta\mathbf{x}$ of the second set of experiments. The LHS and RHS
225 agree to to about -3.42×10^{-15} for the 7-day simulation and about 2.66×10^{-15} for the 31-day simulation (Table 2).

The results shown in Table 2 obtained from the experiments based on Eq. (11) confirm that the MPAS- CO_2 adjoint model has been correctly developed with regard to the TL model. As the TL model has already been confirmed correct with respect to the forward model, it follows that both TL and adjoint models are correct with respect to the forward model of MPAS- CO_2 .
230 This validation ensures the reliability and integrity of the entire MPAS- CO_2 system, including the forward, TL, and adjoint models, as described in this paper and Zheng et al. (2021). It allows MPAS- CO_2 to be used as the basis of a variational assimilation system for carbon flux estimation and as a platform for conducting sensitivity analyses in atmospheric carbon research.

Table 3 presents the computational cost of model simulations using the MPAS- CO_2 system. Using the global 120-480 km
235 VR mesh (Fig. 1; 15898 cells), the 1-month forward model simulation completes in 20 minutes when using 128 processors. Both the TL and adjoint model simulations using the same configuration take approximately 10% longer, indicating that the majority of the computation time is used for integrating the meteorological fields. Furthermore, we conducted another set of 1-month simulations using the models on a global quasi-uniform resolution (UR) mesh of about 120 km, consisting of a total of 40,962 cells. Table 3 demonstrates that the simulations with the VR mesh reduce the computational cost by over 50% for all



240 three models, primarily due to its substantially smaller number of cells. This reduction in computation cost, while preserving the high resolution over areas of interest, should prove advantageous when the models are applied in variational assimilation problems, which typically require many iterations of forward and adjoint model runs.

5 Adjoint sensitivity analysis

245 In addition to forming a key component of variational assimilation systems (Baker et al., 2006; Zheng et al., 2018; Tian and Zou, 2021), adjoint models are powerful tools for sensitivity analysis (Errico and Vukicevic, 1992; Errico, 1997; Zou et al., 1997; Tian and Zou, 2020). Studies focused on carbon flux estimation are often interested in exploring the sensitivity of atmospheric CO₂ measurements to surface CO₂ fluxes; these maps are commonly referred to as observation influence functions or footprints (Cui et al., 2022). The computation of observation footprints using forward models requires a large number of
250 model runs, making it impractical, except at coarse horizontal resolutions. In contrast, adjoint models can calculate observation footprints much more efficiently. For point measurements, such as those from tower data, Lagrangian dispersion models offer an efficient alternative for obtaining footprints (Lin et al., 2003; Stohl et al., 2005). For an example of this, see the publicly available CO₂ observation footprints from Carbon Tracker- Lagrange (CT-L) (Hu et al., 2019), which are generated using the Lagrangian particle dispersion model STILT (Lin et al., 2003), driven by meteorology generated by the Weather Research
255 and Forecast (WRF) model (Skamarock et al., 2008). This approach involves releasing a certain number of particles from the observation location/height and tracing their backward transport in time. Note that CT-L is a regional modeling system that only provides observation footprints within the latitude range 10°-80° N and longitude 0°-180° W for up to 10 days backward in time.

260 In this section, we perform sensitivity analyses using the MPAS-CO₂ adjoint model, which employs backward-in-time integration to calculate two quantities: (1) the sensitivity of atmospheric CO₂ to the model's initial CO₂ mixing ratio, and (2) the sensitivity to the surface flux scaling factor. When a uniform time-invariant surface flux is used, the sensitivity to the surface flux scaling factor calculated by the MPAS-CO₂ adjoint model is the observation footprint. To facilitate comparison with CT-L footprints, the MPAS-CO₂ adjoint model simulations conducted in this section use uniform time-invariant CO₂ surface fluxes
265 of 1.0 μmol/(m² s) for all surface cells, including both land and ocean cells.

First, we conduct MPAS-CO₂ adjoint model simulations for *in situ* CO₂ observations at two towers in the United States: WKT, located at Moody, Texas (31.31° N, 97.33° W), and WGC, located at Walnut Grove, California (38.26° N, 121.49° W). For each tower, the adjoint model is initialized at 00:00 UTC on March 31, 2018. We add an adjoint forcing of 1 ppm CO₂
270 at that time to the model grid cell closest to the tower location and the intake height (475m at WKT and 483m at WGC). The forcing is turned off for subsequent time steps and the adjoint model is run backward in time for 30 days, ending at 00:00 UTC on March 1, 2018. The resulting sensitivity of CO₂ at the WKT tower to the model's CO₂ mixing ratio, which is 3-dimensional,



is shown as a column average in the left panel of Fig. 2. The right panel of Fig. 2 shows the observation footprint (sensitivity to the surface flux scaling factor) at the corresponding times. The figures show that the sensitivity to the initial CO₂ is highest and concentrated closest to the tower site at the time closest to the measurement: 5-days. With the increasing length of the backward-in-time integration, the sensitivity spreads over a larger area and its magnitude decreases. After 30 days, the sensitivity to the initial condition has propagated across most of the northern hemisphere. Figure 2 also indicates that the variation in the sensitivity magnitude decreases with time. To examine this, we calculated the standard deviation (σ) of sensitivity for each day of the 30-day period (Figure 3). The triangles in Fig. 3 show that the magnitude of the standard deviation of sensitivity to the CO₂ mixing ratio decreases rapidly with time for both towers. On the other hand, the sensitivity to the surface flux scaling factor (footprint) exhibits a different pattern from the sensitivity to the initial CO₂. As shown in Fig. 2, the footprint spread spatially but the near field to the tower maintains a much higher magnitude than the far fields. By the end of 30 days, the footprint of WKT tower covers almost the entire northern hemisphere, with the area north and northwest of the tower within the conterminous United States exhibiting a much higher magnitude than the more distant area. The circles in Fig. 3 indicate that the standard deviation of the footprint increase with time, but the rate of increase diminishes substantially after about 10 to 15 days. The finding suggests that extending the adjoint model integration further backward in time will still result in changes to the footprint, but with a much-reduced change rate.

For comparison, in Figure 4 we plot the MPAS-CO₂ adjoint model-calculated 10-day footprints in the CT-L geographic domain. The figure reveals that the MPAS-CO₂ adjoint model-calculated WKT tower footprint spans most of the western and northwestern United States, with the highest sensitivity in Texas, Missouri, Iowa, Kansas, and Nebraska. Additionally, the footprint extends to a substantial area over the northeastern Pacific Ocean. The spatial pattern of the CT-L calculated footprint (Fig. 4c) is similar to that from the MPAS-CO₂ adjoint model, but it is visibly less continuous. Fig. 4 also shows that the MPAS-CO₂ adjoint model-calculated footprint for the WGC tower covers northern California, southwestern Washington, and a portion of the northeastern Pacific Ocean. The CT-L-calculated footprint exhibits a similar spatial pattern and magnitude. Overall, both the MPAS-CO₂ adjoint model and CT-L provide valuable information on the sensitivity of atmospheric CO₂ measurements to the surface flux: similar spatial patterns although with some differences due to resolution and the Lagrangian/Eulerian framework difference.

In the second set of experiments, we compare CT-L and MPAS-CO₂ adjoint model footprints for a swath of OCO-2 X_{CO₂} measurements. The ground track of the OCO-2 orbit used in the experiments is indicated by the blue color line in Fig. 1. This orbit crosses North America from the Caribbean Sea to Canada's Northwest Territories in a northward direction between 18:31 UTC and 18:48 UTC on June 30, 2106. Since OCO-2 X_{CO₂} represents the column average of atmospheric CO₂, CT-L calculates X_{CO₂} footprints at 14 discrete height levels, ranging from 50 to 14,000 meters above the ground. For each height level, footprints are computed by placing a number of particles at that specific height. To ensure consistency with the CT-L approach, the MPAS-CO₂ adjoint model is configured to apply the adjoint forcing at the corresponding vertical levels within the model. This configuration allows for a direct comparison between the footprints calculated by the MPAS-CO₂ adjoint model and the



CT-L footprints.

310 In the top panel of Fig. 5, we present the footprints of a point located south of Jamaica in the Caribbean Sea (17.82°N, 77.88°W) at 500 m above the surface. Both the MPAS-CO₂ adjoint model and CT-L footprints largely extend eastward over the Atlantic Ocean, indicating transport from the surface due to the influence of the easterly trade winds. Additionally, the MPAS-CO₂ adjoint model-calculated footprint includes a branch that crosses the equator and extends southeastward to the southern hemisphere between 30°W and 40°W longitude. This feature is not shown in the CT-L footprint due to its limited-
315 area domain. In the lower panel of Fig. 5, we present the footprint of the same location but at 10,000 m above the surface. Both the MPAS-CO₂ adjoint and CT-L footprints show a primarily counterclockwise extension, covering the Gulf of Mexico and Texas. Moreover, there is a second segment extending westward from Texas toward the west coast. Upon closer examination, we observe that the CT-L-calculated footprint has a higher magnitude than the MPAS-CO₂ adjoint model over the Gulf of Mexico, but a lower magnitude over the mid-Atlantic regions of the United States, including from Kentucky to the Carolinas.
320 The distinct patterns in both systems' footprints at different vertical levels (500m and 10,000m) indicate significant differences in horizontal and vertical transport patterns.

Figure 6 shows the corresponding footprints for an OCO-2 X_{CO₂} location in eastern Kentucky (36.8°N, 82.9°W) for particles released at 2,000 and 4,500m above the ground, respectively. The footprint of 2,000m extends predominantly northward,
325 covering the Great Lakes region and part of the Canadian Shield. In comparison, the footprint for 4,500m is mostly directed to the west. Another notable difference is that the highest magnitude portion of the 2,000m footprint is in close proximity to the point, while the 4,500m footprint is not in proximity to the point at all. These differences between the two height levels are evident in both the MPAS-CO₂ adjoint model and CT-L calculated footprints. In Fig. 7, we show the footprint of an OCO-2 sounding location on the southwest coast of Hudson Bay, Canada (56.96°N, 91.89°W) at 500m and 4,500m altitude. Both the
330 MPAS-CO₂ adjoint and CT-L footprints for 500m are generally confined near to the sounding location, indicating that local surface fluxes have a significant influence on the atmospheric CO₂ at 500m above the surface. In comparison, the footprint of 4,500m is located more than 2,000km northwestward, mostly covering Alaska; the particles move that far horizontally in the time it takes them to advect and mix 4,500m in the vertical. These findings emphasize the significant impact of vertical mixing on the spatial distribution of footprint at different altitudes, highlighting the unique patterns of horizontal and vertical transport
335 in each case.

In additional MPAS-CO₂ adjoint model runs, we quantitatively compare the footprints of the entire OCO-2 track at each of the 14 height levels with the CT-L footprints. This comparison is conducted by performing a single MPAS-CO₂ adjoint model run to calculate the footprint at the end of the 10-day backward-in-time integration for each height level. We then compare these
340 resulting footprints with their CT-L counterparts. Figure 8 shows the comparison at 4 height levels: 500m, 2,000m, 5,500m, and 10,000 m above the surface. The figure reveals that the footprints calculated by the two systems have similar spatial patterns within the limited-area domain of CT-L. However, it is important to note that a substantial portion of the footprints extends



beyond the CT-L domain. For instance, the footprints of 2,000m and 5,500m levels have significant coverage over Russian Siberia, while the footprint of the 10,000m level extends from the eastern Pacific Ocean to northeastern and western China, both of which are outside the CT-L model domain.

In order to compare the footprints from the two systems quantitatively, we aggregated the footprints onto a $2^\circ \times 3^\circ$ (lat \times lon) grid within the area covered by the CT-L model domain for each of the 14 height levels. Figure 9 shows the comparison for each of the 14. In the figure, the CT-L calculated footprints are on the X-axis, and MPAS-CO₂ adjoint model calculated footprints are on the Y-axis. The figure demonstrates that the agreement between the two systems is better for footprints at lower heights than at higher heights. Specifically, at lower heights ranging from 500m to 2,500m, the MPAS-CO₂ adjoint model calculated footprints tend to have a somewhat higher magnitude than CT-L. However, at higher heights from 4,500m to 14,000m, the footprints calculated by CT-L tend to be of much higher magnitude compared to the MPAS-CO₂ adjoint model. These differences in magnitude between the two systems could be attributed to various factors, including differences in model configurations, spatial resolution, and treatment of vertical mixing processes. Previous studies have shown that Lagrangian models, such as CT-L, can sometimes have different vertical mixing behavior compared to Eulerian models, especially at high altitudes (Karion et al., 2019).

In a final experiment, we use the MPAS-CO₂ adjoint model to examine the impact of different vertical distributions on footprint calculation. Two adjoint model simulations are conducted for the OCO-2 orbit that crosses South America and North America between 17:36 UTC and 18:13 UTC on August 23, 2016 (the red color track in Fig. 1). Both simulations have the same adjoint forcing of 1 ppm X_{CO_2} added at 18:00 UTC on August 23, 2016, and running backward in time for 30 days. The key difference between the two simulations lies in the vertical distributions of the adjoint forcing. For the first simulation, we adopt profile 1, which is obtained by combining the X_{CO_2} averaging kernel and pressure weight function (O'Dell et al., 2018). In contrast, profile 2 prioritizes X_{CO_2} information in the lower part of the troposphere (Figure 10). This experiment aims to highlight how these differences in vertical distribution impact the footprint calculation, leading to variations in flux estimation using variational assimilation. The results of this experiment will provide valuable insights to the importance of selecting appropriate vertical distribution when using the adjoint model for CO₂ flux estimation.

The top two panels of Fig. 11 show the footprints resulting from MPAS-CO₂ adjoint model simulations using the two distinct vertical distribution profiles for the adjoint forcing (Fig. 10). Although the two footprints may initially appear very similar, substantial differences become evident as shown in the bottom panel in Fig. 11. Specifically, the footprint calculated using Profile 1 exhibits lower magnitudes compared to that obtained using Profile 2 in most extratropical regions in both the North Hemisphere and Southern Hemisphere. Conversely, in most of the tropics, the footprint calculated using Profile 1 shows higher magnitudes than for Profile 2. Profile 2, which allocates more adjoint forcing to the lower atmosphere and less to the upper atmosphere, appears to be more sensitive to the stronger convective transport of surface CO₂ flux in the tropics than in the extratropics. These convective transport differences can account for the observed variations in the footprints between the two



profiles. These findings underscore the critical importance of selecting an appropriate vertical distribution for the model-data difference when using an adjoint model during variational assimilation.

380 6 Conclusions

The MPAS-CO₂ system consists of forward, TL, and adjoint models that are built upon the variable-resolution capability of the compressible non-hydrostatic MPAS-A model (Skamarock et al., 2012). It promises to be a useful tool for carbon flux inverse modeling at the global and regional scales. The forward model of MPAS-CO₂ is documented by Zheng et al. (2021). In this paper, we focus on the development of its tangent linear and adjoint models. Through rigorous testing, we have confirmed
385 the correctness and accuracy of the newly developed MPAS-CO₂ TL and adjoint models. A key challenge in developing the adjoint model was efficiently accessing meteorological variables during the model's backward-in-time integration. We have successfully implemented a strategy that combines recalculation and storage of meteorological variables. This approach significantly reduces the memory requirement, making the adjoint model feasible for long simulations, which are often necessary for CO₂ inverse modeling.

390

The results of the sensitivity analysis using the newly developed MPAS-CO₂ adjoint model provide valuable insights for designing CO₂ data assimilation systems. The increasing homogeneity of the sensitivity to the initial atmosphere CO₂ mixing ratio with longer integration length highlights the importance of selecting an appropriate assimilation window length. The comparison of the CO₂ observation footprints between the MPAS-CO₂ adjoint model and the NOAA CT-L system demonstrates
395 good agreement, validating the accuracy of the adjoint model's footprint calculations. The comparison of OCO-2 X_{CO₂} footprints reveals differences in sensitivity between the two systems at different altitudes. MPAS-CO₂ adjoint model-calculated footprints tend to have higher magnitudes at low altitudes and lower magnitudes at high altitudes compared to CT-L. These differences likely arise from variations in vertical transport between the two systems. Lastly, the sensitivity analysis using two different vertical distribution profiles for adjoint forcing highlights the importance of correctly mapping model-data difference
400 in X_{CO₂} to the transport model's vertical levels.

In addition to being a powerful tool for sensitivity analysis, the adjoint model plays a critical role in CO₂ variational data assimilation. Our future research efforts will focus on integrating the forward and adjoint models of MPAS-CO₂ into such a system. This integration has the potential to bridge a significant gap by establishing an online Eulerian transport model-based
405 global variational assimilation system for CO₂ that targets high resolution in critical regions while at the same time avoiding the pitfalls associated with the lateral boundaries needed in regional-domain inversions.



Code and data availability

The MPAS-CO₂ TL and adjoint models v7.3 developed in this paper can be downloaded from the CERN-based Zenodo archive at <https://doi.org/10.5281/zenodo.8226620>. This includes the model source code, instructions for compilation, and
410 example script for running models. Instructions for how to compile and run the models are provided in the package. CarbonTracker CO₂ flux and posterior mixing ratio data can be obtained from the NOAA website: <https://www.esrl.noaa.gov/gmd/ccgg/carbontracker/download.php>. CT-L footprints can be obtained from the NOAA website: <https://gml.noaa.gov/ccgg/carbontracker-lagrange/>

Author contributions

415 TZ designed and developed the MPAS-CO₂ TL and adjoint models. XT generated the 120-480km VR mesh used in model simulations. TZ, SF, JS, and XT designed and carried out the model accuracy verification experiments. TZ, SF, DB, and MB designed the adjoint sensitivity analysis experiments. All authors contributed to writing the paper.

Competing interests

The authors declare that they have no conflict of interest.

420 Acknowledgment

We thank the MPAS development team for making their code available to the public; We thank Dr. Bill Skamarock for his advice regarding the MPAS-A advection scheme. The model developments and simulations were carried out using Michigan State University High-Performance Computing Center (HPCC). PNNL is operated by the US Department of Energy by the Battelle Memorial Institute under contract DE-A05-76RL01830.

425 7 Financial support

This research has been supported by the National Aeronautics and Space Administration Carbon Monitoring System (CMS) grant no. 80HQTR21T0069.



References

- Agusti-Panareda, A., Diamantakis, M., Massart, S., Chevallier, F., Munoz-Sabater, J., Barre, J., Curcoll, R., Engelen, R., Langerock, B., Law, R. M., Loh, Z., Anton Morgui, J., Parrington, M., Pench, V.-H., Ramonet, M., Roehl, C., Vermeulen, A. T., Warneke, T., and Wunch, D.: Modelling CO₂ weather - why horizontal resolution matters, *Atmospheric Chemistry and Physics*, 19, 7347–7376, <https://doi.org/10.5194/acp-19-7347-2019>, 2019.
- Baker, D. F., Doney, S. C., and Schimel, D. S.: Variational data assimilation for atmospheric CO₂, *Tellus B*, 58, 359–365, 2006.
- Byrne, B., Baker, D. F., Basu, S., Bertolacci, M., Bowman, K. W., Carroll, D., Chatterjee, A., Chevallier, F., Ciais, P., Cressie, N., Crisp, D., Crowell, S., Deng, F., Deng, Z., Deutscher, N. M., Dubey, M. K., Feng, S., García, O. E., Griffith, D. W. T., Herkommer, B., Hu, L., Jacobson, A. R., Janardanan, R., Jeong, S., Johnson, M. S., Jones, D. B. A., Kivi, R., Liu, J., Liu, Z., Maksyutov, S., Miller, J. B., Miller, S. M., Morino, I., Notholt, J., Oda, T., O'Dell, C. W., Oh, Y.-S., Ohyama, H., Patra, P. K., Peiro, H., Petri, C., Philip, S., Pollard, D. F., Poulter, B., Remaud, M., Schuh, A., Sha, M. K., Shiomi, K., Strong, K., Sweeney, C., Té, Y., Tian, H., Velazco, V. A., Vrekoussis, M., Warneke, T., Worden, J. R., Wunch, D., Yao, Y., Yun, J., Zammit-Mangion, A., and Zeng, N.: National CO₂ budgets (2015–2020) inferred from atmospheric CO₂ observations in support of the global stocktake, *Earth System Science Data*, 15, 963–1004, <https://doi.org/10.5194/essd-15-963-2023>, 2023.
- Courtier, P., Thepaut, J. N., and Hollingsworth, A.: A Strategy for Operational Implementation of 4d-Var, Using an Incremental Approach, *Quart. J. Roy. Meteor. Soc.*, 120, 1367–1387, b, 1994.
- Cui, Y. Y., Zhang, L., Jacobson, A. R., Johnson, M. S., Philip, S., Baker, D., Chevallier, F., Schuh, A. E., Liu, J., Crowell, S., et al.: Evaluating Global Atmospheric Inversions of Terrestrial Net Ecosystem Exchange CO₂ Over North America on Seasonal and Sub-Continental Scales, *Geophysical Research Letters*, 49, e2022GL100147, 2022.
- Errico, R. M.: What is an adjoint model?, *Bulletin of the American Meteorological Society*, 78, 2577–2592, 1997.
- Errico, R. M. and Vukicevic, T.: Sensitivity analysis using an adjoint of the PSU-NCAR mesoseale model, *Monthly weather review*, 120, 1644–1660, 1992.
- Feng, S., Lauvaux, T., Newman, S., Rao, P., Ahmadov, R., Deng, A., Diaz-Isaac, L. I., Duren, R. M., Fischer, M. L., Gerbig, C., Gurney, K. R., Huang, J., Jeong, S., Li, Z., Miller, C. E., O'Keefe, D., Patarasuk, R., Sander, S. P., Song, Y., Wong, K. W., and Yung, Y. L.: Los Angeles megacity: a high-resolution land-atmosphere modelling system for urban CO₂ emissions, *Atmospheric Chemistry and Physics*, 16, 9019–9045, <https://doi.org/10.5194/acp-16-9019-2016>, 2016.
- Giering, R. and Kaminski, T.: Recipes for adjoint code construction, *ACM Trans. Math. Software*, 24, 437–474, 1998.
- Giering, R., Kaminski, T., Todling, R., Errico, R., Gelaro, R., and Winslow, N.: Tangent Linear and Adjoint Versions of NASA/GMAO's Fortran 90 Global Weather Forecast Model, *Automatic Differentiation: Applications, Theory, and Implementations*, pp. 275–284, 2006.
- Giles, M. B. and Pierce, N. A.: An introduction to the adjoint approach to design, *Flow, turbulence and combustion*, 65, 393–415, 2000.
- Grell, G., Freitas, S. R., Stuefer, M., and Fast, J.: Inclusion of biomass burning in WRF-Chem: impact of wildfires on weather forecasts, *Atmospheric Chemistry and Physics*, 11, 5289–5303, <https://doi.org/10.5194/acp-11-5289-2011>, 2011.
- Grell, G. A., Peckham, S. E., Schmitz, R., McKeen, S. A., Frost, G., Skamarock, W. C., and Eder, B.: Fully coupled online chemistry within the WRF model, *Atmospheric Environment*, 39, 6957–6975, 2005.
- Guerrette, J. J. and Henze, D. K.: Development and application of the WRFPLUS-Chem online chemistry adjoint and WRFDA-Chem assimilation system, *Geosci. Model Dev.*, 8, 1857–1876, 2015.



- 465 Hascoet, L. and Pascual, V.: The Tapenade Automatic Differentiation Tool: Principles, Model, and Specification, *ACM Trans. Math. Software*, 39, 20, 2013.
- Henze, D. K., Hakami, A., and Seinfeld, J. H.: Development of the adjoint of GEOS-Chem, *Atmospheric Chemistry and Physics*, 7, 2413–2433, <https://doi.org/10.5194/acp-7-2413-2007>, 2007.
- Hoffmann, L., Günther, G., Li, D., Stein, O., Wu, X., Griessbach, S., Heng, Y., Konopka, P., Müller, R., Vogel, B., and Wright, J. S.: From ERA-Interim to ERA5: the considerable impact of ECMWF’s next-generation reanalysis on Lagrangian transport simulations, *Atmospheric Chemistry and Physics*, 19, 3097–3124, <https://doi.org/10.5194/acp-19-3097-2019>, 2019.
- 470 Hong, S.-Y., Noh, Y., and Dudhia, J.: A new vertical diffusion package with an explicit treatment of entrainment processes, *Monthly Weather Review*, 134, 2318–2341, <https://doi.org/10.1175/MWR3199.1>, 2006.
- Hu, L., Andrews, A. E., Thoning, K. W., Sweeney, C., Miller, J. B., Michalak, A. M., Dlugokencky, E., Tans, P. P., Shiga, Y. P., Mountain, M., Nehrkorn, T., Montzka, S. A., McKain, K., Kofler, J., Trudeau, M., Michel, S. E., Biraud, S. C., Fischer, M. L., Worthy, D. E. J., 475 Vaughn, B. H., White, J. W. C., Yadav, V., Basu, S., and van der Velde, I. R.: Enhanced North American carbon uptake associated with El Niño, *Science Advances*, 5, <https://doi.org/10.1126/sciadv.aaw0076>, 2019.
- Hurt, G. C., Andrews, A., Bowman, K., Brown, M. E., Chatterjee, A., Escobar, V., Fatoyinbo, L., Griffith, P., Guy, M., Healey, S. P., et al.: The NASA carbon monitoring system phase 2 synthesis: scope, findings, gaps and recommended next steps, *Environmental Research Letters*, 2022.
- 480 Jacobson, A. R., Schuldt, K. N., Miller, J. B., Oda, T., Tans, P., Arlyn Andrews, Mund, J., Ott, L., Collatz, G. J., Aalto, T., Afshar, S., Aikin, K., Aoki, S., Apadula, F., Baier, B., Bergamaschi, P., Beyersdorf, A., Biraud, S. C., Bollenbacher, A., Bowling, D., Brailsford, G., Abshire, J. B., Chen, G., Huilin Chen, Lukasz Chmura, Sites Climadat, Colomb, A., Conil, S., Cox, A., Cristofanelli, P., Cuevas, E., Curcoll, R., Sloop, C. D., Davis, K., Wekker, S. D., Delmotte, M., DiGangi, J. P., Dlugokencky, E., Ehleringer, J., Elkins, J. W., Emmenegger, L., Fischer, M. L., Forster, G., Frumau, A., Galkowski, M., Gatti, L. V., Gloor, E., Griffis, T., Hammer, S., Haszpra, L., Hatakka, J., Heliasz, 485 M., Hensen, A., Hermanssen, O., Hints, E., Holst, J., Jaffe, D., Karion, A., Kawa, S. R., Keeling, R., Keronen, P., Kolari, P., Kominkova, K., Kort, E., Krummel, P., Kubistin, D., Labuschagne, C., Langenfelds, R., Laurent, O., Laurila, T., Lauvaux, T., Law, B., Lee, J., Lehner, I., Leuenberger, M., Levin, I., Levula, J., Lin, J., Lindauer, M., Loh, Z., Lopez, M., Myhre, C. L., Machida, T., Mammarella, I., Manca, G., Manning, A., Manning, A., Marek, M. V., Marklund, P., Martin, M. Y., Matsueda, H., McKain, K., Meijer, H., Meinhardt, F., Miles, N., Miller, C. E., Mölder, M., Montzka, S., Moore, F., Josep-Anton Morgui, Morimoto, S., Munger, B., Jaroslaw Necki, Newman, S., 490 Nichol, S., Niwa, Y., O’Doherty, S., Mikael Ottosson-Löfvenius, Paplawsky, B., Peischl, J., Peltola, O., Jean-Marc Pichon, Piper, S., Plass-Dölmer, C., Ramonet, M., Reyes-Sanchez, E., Richardson, S., Riris, H., Ryerson, T., Saito, K., Sargent, M., Sasakawa, M., Sawa, Y., Say, D., Scheeren, B., Schmidt, M., Schmidt, A., Schumacher, M., Shepson, P., Shook, M., Stanley, K., Steinbacher, M., Stephens, B., Sweeney, C., Thoning, K., Torn, M., Turnbull, J., Tørseth, K., Bulk, P. V. D., Laan-Luijckx, I. T. V. D., Dinker, D. V., Vermeulen, A., Viner, B., Vitkova, G., Walker, S., Weyrauch, D., Wofsy, S., Worthy, D., Dickon Young, and Miroslaw Zimnoch: CarbonTracker CT2019, 495 <https://doi.org/10.25925/39M3-6069>, 2020.
- Kain, J. S.: The Kain–Fritsch Convective Parameterization: An Update, *Journal of Applied Meteorology*, 43, 170–181, [https://doi.org/10.1175/1520-0450\(2004\)043<0170:TKCPAU>2.0.CO;2](https://doi.org/10.1175/1520-0450(2004)043<0170:TKCPAU>2.0.CO;2), 2004.
- Karion, A., Lauvaux, T., Lopez Coto, I., Sweeney, C., Mueller, K., Gourdji, S., Angevine, W., Barkley, Z., Deng, A., Andrews, A., et al.: Intercomparison of atmospheric trace gas dispersion models: Barnett Shale case study, *Atmospheric Chemistry and Physics*, 19, 2561–500 2576, 2019.



- Kawa, S. R., Erickson, D. J., Pawson, S., and Zhu, Z.: Global CO₂ transport simulations using meteorological data from the NASA data assimilation system, *Journal of Geophysical Research-Atmospheres*, 109, d18312, 2004.
- Kopacz, M., Jacob, D. J., Henze, D. K., Heald, C. L., Streets, D. G., and Zhang, Q.: Comparison of adjoint and analytical Bayesian inversion methods for constraining Asian sources of carbon monoxide using satellite (MOPITT) measurements of CO columns, *Journal of Geophysical Research-Atmospheres*, 114, d04305, 2009.
- 505 Krol, M., Houweling, S., Bregman, B., van den Broek, M., Segers, A., van Velthoven, P., Peters, W., Dentener, F., and Bergamaschi, P.: The two-way nested global chemistry-transport zoom model TM5: algorithm and applications, *Atmospheric Chemistry and Physics*, 5, 417–432, <https://doi.org/10.5194/acp-5-417-2005>, 2005.
- Lauvaux, T., Schuh, A. E., Uliasz, M., Richardson, S., Miles, N., Andrews, A. E., Sweeney, C., Diaz, L. I., Martins, D., Shepson, P. B., and Davis, K. J.: Constraining the CO₂ budget of the corn belt: exploring uncertainties from the assumptions in a mesoscale inverse system, *Atmospheric Chemistry and Physics*, 12, 337–354, <https://doi.org/10.5194/acp-12-337-2012>, 2012.
- 510 Lin, J. C., Gerbig, C., Wofsy, S. C., Andrews, A. E., Daube, B. C., Davis, K. J., and Grainger, C. A.: A near-field tool for simulating the upstream influence of atmospheric observations: The Stochastic Time-Inverted Lagrangian Transport (STILT) model, *Journal of Geophysical Research-Atmospheres*, 108, 4493, 2003.
- 515 Meirink, J. F., Eskes, H. J., and Goede, A. P. H.: Sensitivity analysis of methane emissions derived from SCIAMACHY observations through inverse modelling, *Atmospheric Chemistry and Physics*, 6, 1275–1292, 2006.
- Meirink, J. F., Bergamaschi, P., Frankenberg, C., d’Amelio, M. T. S., Dlugokencky, E. J., Gatti, L. V., Houweling, S., Miller, J. B., Roekmann, T., Villani, M. G., and Krol, M. C.: Four-dimensional variational data assimilation for inverse modeling of atmospheric methane emissions: Analysis of SCIAMACHY observations, *Journal of Geophysical Research-Atmospheres*, 113, d17301, 2008.
- 520 O’Dell, C. W., Eldering, A., Wennberg, P. O., Crisp, D., Gunson, M. R., Fisher, B., Frankenberg, C., Kiel, M., Lindqvist, H., Mandrake, L., Merrelli, A., Natraj, V., Nelson, R. R., Osterman, G. B., Payne, V. H., Taylor, T. R., Wunch, D., Drouin, B. J., Oyafuso, F., Chang, A., McDuffie, J., Smyth, M., Baker, D. F., Basu, S., Chevallier, F., Crowell, S. M. R., Feng, L., Palmer, P. I., Dubey, M., García, O. E., Griffith, D. W. T., Hase, F., Iraci, L. T., Kivi, R., Morino, I., Notholt, J., Ohyama, H., Petri, C., Roehl, C. M., Sha, M. K., Strong, K., Sussmann, R., Te, Y., Uchino, O., and Velasco, V. A.: Improved Retrievals of Carbon Dioxide from the Orbiting Carbon Observatory-2 with the version 8 ACOS algorithm, *Atmospheric Measurement Techniques Discussions*, 2018, 1–57, <https://doi.org/10.5194/amt-2018-257>, 2018.
- 525 Pillai, D., Gerbig, C., Kretschmer, R., Beck, V., Karstens, U., Neininger, B., and Heimann, M.: Comparing Lagrangian and Eulerian models for CO₂ transport – a step towards Bayesian inverse modeling using WRF/STILT-VPRM, *Atmospheric Chemistry and Physics*, 12, 8979–8991, <https://doi.org/10.5194/acp-12-8979-2012>, 2012.
- Rayner, P. J., Michalak, A. M., and Chevallier, F.: Fundamentals of data assimilation applied to biogeochemistry, *Atmospheric Chemistry and Physics*, 19, 13911–13932, <https://doi.org/10.5194/acp-19-13911-2019>, 2019.
- 530 Schuh, A. E., Otte, M., Lauvaux, T., and Oda, T.: Far-field biogenic and anthropogenic emissions as a dominant source of variability in local urban carbon budgets: A global high-resolution model study with implications for satellite remote sensing, *Remote Sensing of Environment*, 262, 112473, 2021.
- Skamarock, W., Klemp, J., Dudhia, J., Gill, D., Barker, D., Duda, M., Huang, X., Wang, W., and Powers, J.: A description of the Advanced Research WRF version 3, NCAR Tech Note NCAR/TN-475+STR, 2008.
- 535 Skamarock, W. C. and Gassmann, A.: Conservative Transport Schemes for Spherical Geodesic Grids: High-Order Flux Operators for ODE-Based Time Integration, *Monthly Weather Review*, 139, 2962–2975, <https://doi.org/10.1175/MWR-D-10-05056.1>, 2011.



- Skamarock, W. C., Klemp, J. B., Duda, M. G., Fowler, L. D., Park, S.-H., and Ringler, T. D.: A Multiscale Nonhydrostatic Atmospheric Model Using Centroidal Voronoi Tessellations and C-Grid Staggering, *Monthly Weather Review*, 140, 3090–3105, <https://doi.org/10.1175/MWR-D-11-00215.1>, 2012.
- 540 Stohl, A., Forster, C., Frank, A., Seibert, P., and Wotawa, G.: Technical note: The Lagrangian particle dispersion model FLEXPART version 6.2, *Atmospheric Chemistry and Physics*, 5, 2461–2474, 2005.
- Tian, X. and Zou, X.: Development of the tangent linear and adjoint models of the MPAS-Atmosphere dynamic core and applications in adjoint relative sensitivity studies, *Tellus A: Dynamic Meteorology and Oceanography*, 72, 1–17, <https://doi.org/10.1080/16000870.2020.1814602>, 2020.
- 545 Tian, X. and Zou, X.: Validation of a prototype global 4D-Var data assimilation system for the MPAS-atmosphere model, *Monthly Weather Review*, 149, 2803–2817, 2021.
- Walko, R. L. and Avissar, R.: The Ocean-Land-Atmosphere Model (OLAM). Part I: Shallow-Water Tests, *Monthly Weather Review*, 136, 4033–4044, <https://doi.org/10.1175/2008MWR2522.1>, 2008.
- 550 Wang, H., Skamarock, W. C., and Feingold, G.: Evaluation of scalar advection schemes in the Advanced Research WRF model using large-eddy simulations of aerosol-cloud interactions, *Monthly Weather Review*, 137, 2547–2558, 2009.
- Zheng, T., Nassar, R., and Baxter, M.: Estimating power plant CO₂ emission using OCO-2 X_{CO_2} and high resolution WRF-Chem simulations, *Environmental Research Letters*, 14, <https://doi.org/10.1088/1748-9326/ab25ae>, 2019.
- Zheng, T., Feng, S., Davis, K. J., Pal, S., and Morguá, J.: Development and evaluation of CO₂ transport in MPAS-A v6.3, *Geoscientific Model Development*, 14, 3037–3066, <https://doi.org/10.5194/gmd-14-3037-2021>, 2021.
- 555 Zheng, T., French, N. H. F., and Baxter, M.: Development of the WRF-CO₂ 4D-Var assimilation system v1.0, *Geoscientific Model Development*, 11, 1725–1752, <https://doi.org/10.5194/gmd-11-1725-2018>, 2018.
- Zou, X., Vandenbergh, F., Pondeva, M., and Kuo, Y.-H.: Introduction to adjoint techniques and the MM5 adjoint modeling system, NCAR Technical note, 1997.

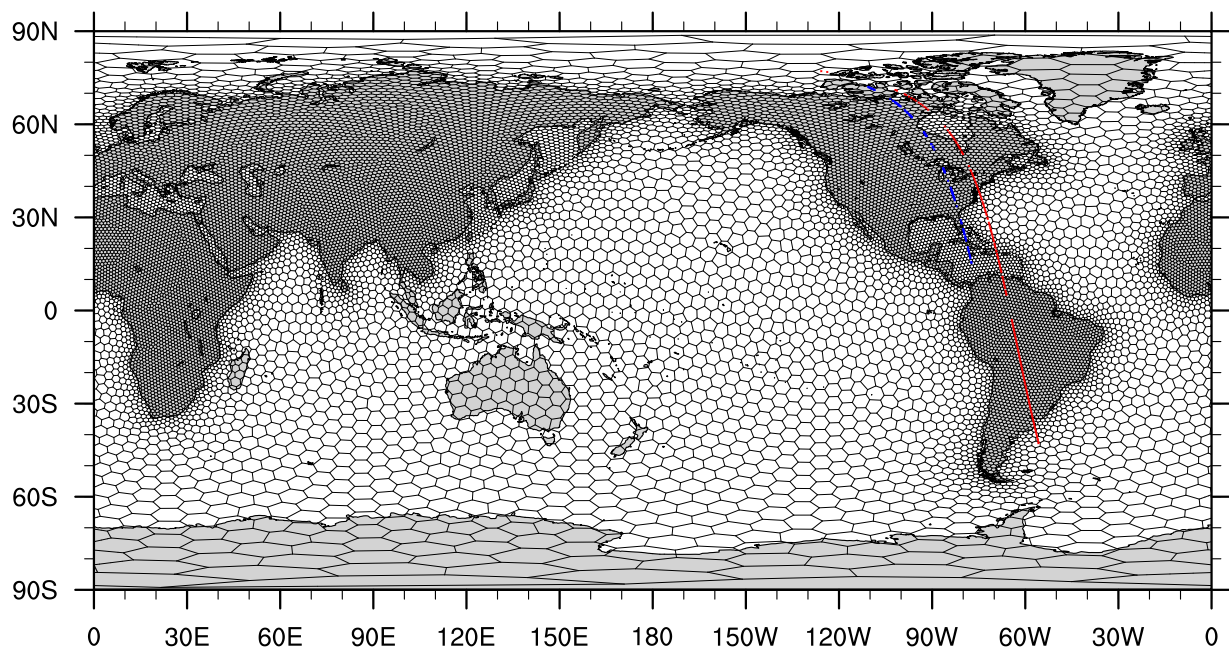


Figure 1. An MPAS-CO₂ global variable resolution mesh ranging from ~120km over most of land regions to ~480km over oceans. Also shown in the figures are the ground tracks of two OCO-2 orbits, which are used for the adjoint sensitivity studies described in Section 5. The blue-colored ground track crosses North America from the Caribbean Sea northward between 18:31 UTC and 18:48 UTC on June 30, 2016. The red-colored ground track crosses from South America to North America between 17:36 UTC and 18:13 UTC on August 23, 2016.

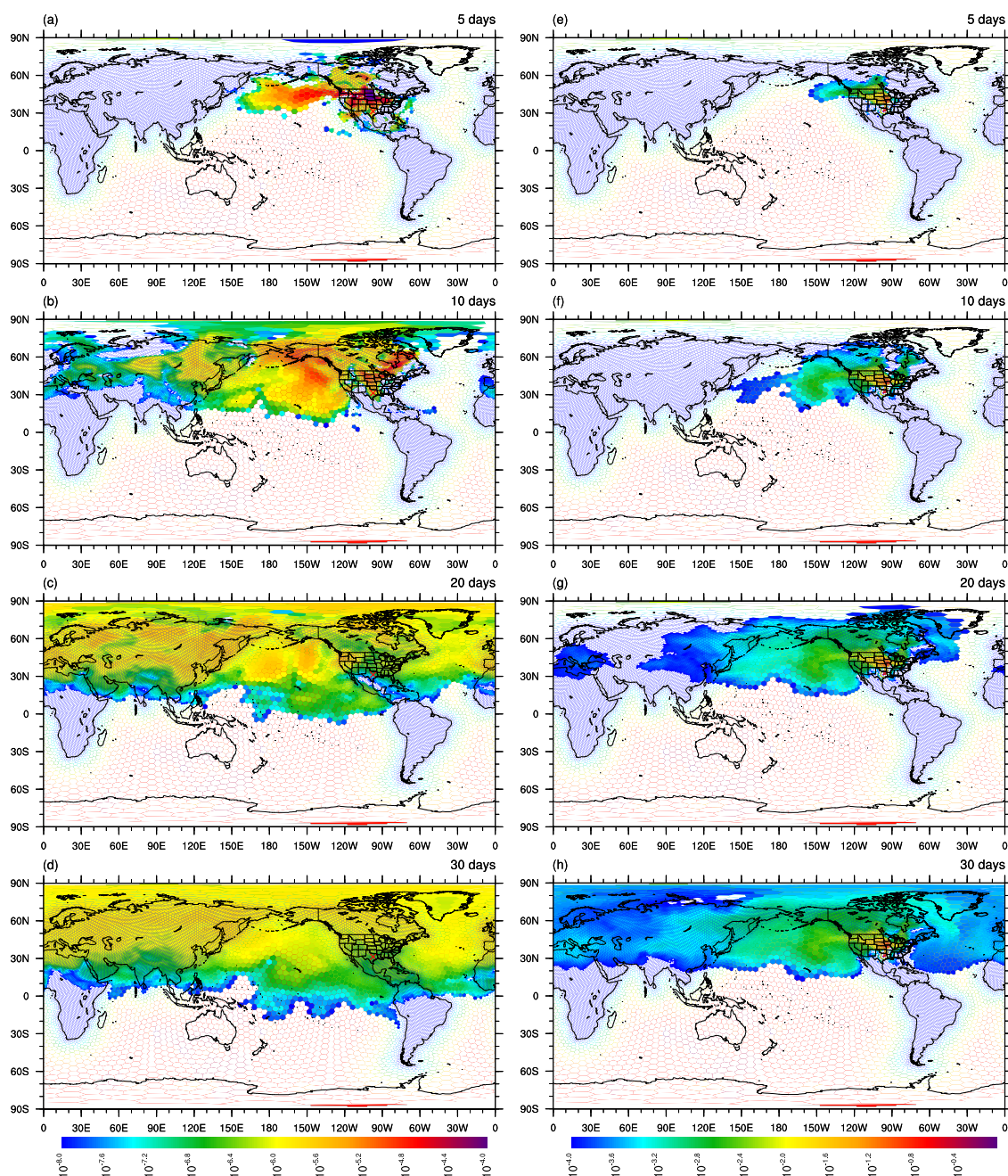


Figure 2. The column average of sensitivity of CO₂ at the WKT tower at 00:00 UTC on March 31 2018 to CO₂ mixing ratio (units: ppm/ppm) at 5, 10, 20, and 30 days backward in time (a)-(d). The WKT tower (31.3149°N, 97.3269°W) measurements used here are taken 457m above the ground level and labeled by the red color cross in the figures of the left column. Figures (e)-(h) are the sensitivity of CO₂ at the tower at the same time to the surface CO₂ flux scaling factor (footprint, units:ppm/ $\mu\text{mol m}^{-2} \text{s}^{-1}$) computed 5, 10, 20, and 30 days backward-in-time, respectively.

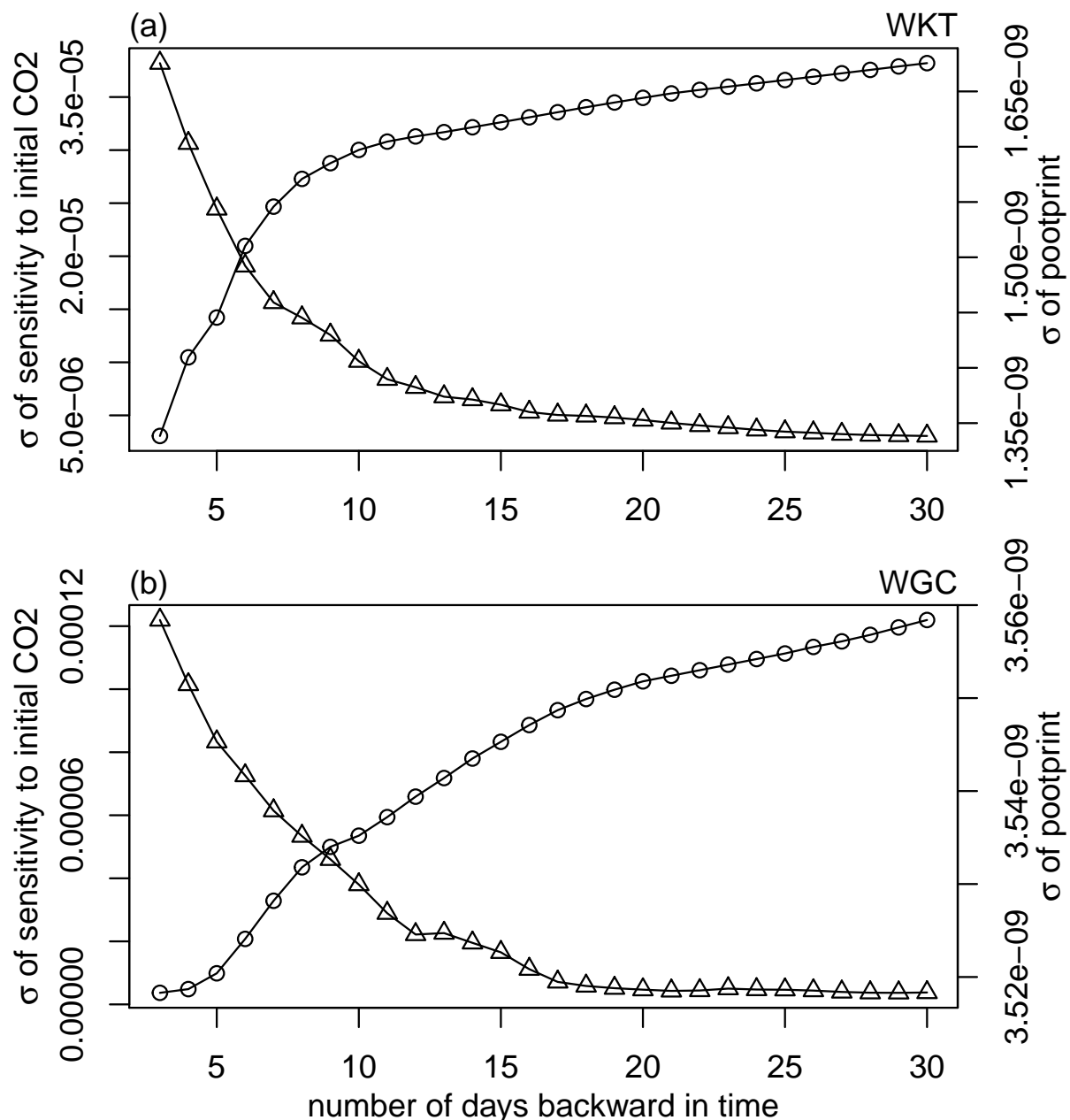


Figure 3. The variation of the standard deviation (σ) of sensitivity to the initial CO₂ and the sensitivity to the flux scaling factor (footprint) over time. The standard deviations were calculated from MPAS-CO₂ adjoint model simulations starting on 2018 March 31 at 00:00 UTC, running 30 days backward in time, and ending on 2018 March 1 at 00:00 UTC. The top panel (a) is for the WKT tower (457 magl) while the bottom panel (b) is for the WGC tower. In each figure, the triangles represent the standard deviation of sensitivity to the CO₂ mixing ratio field (units: ppm/ppm), and the circles represent the standard deviation of footprint (units: ppm/ $\mu\text{mol m}^{-2} \text{s}^{-1}$).

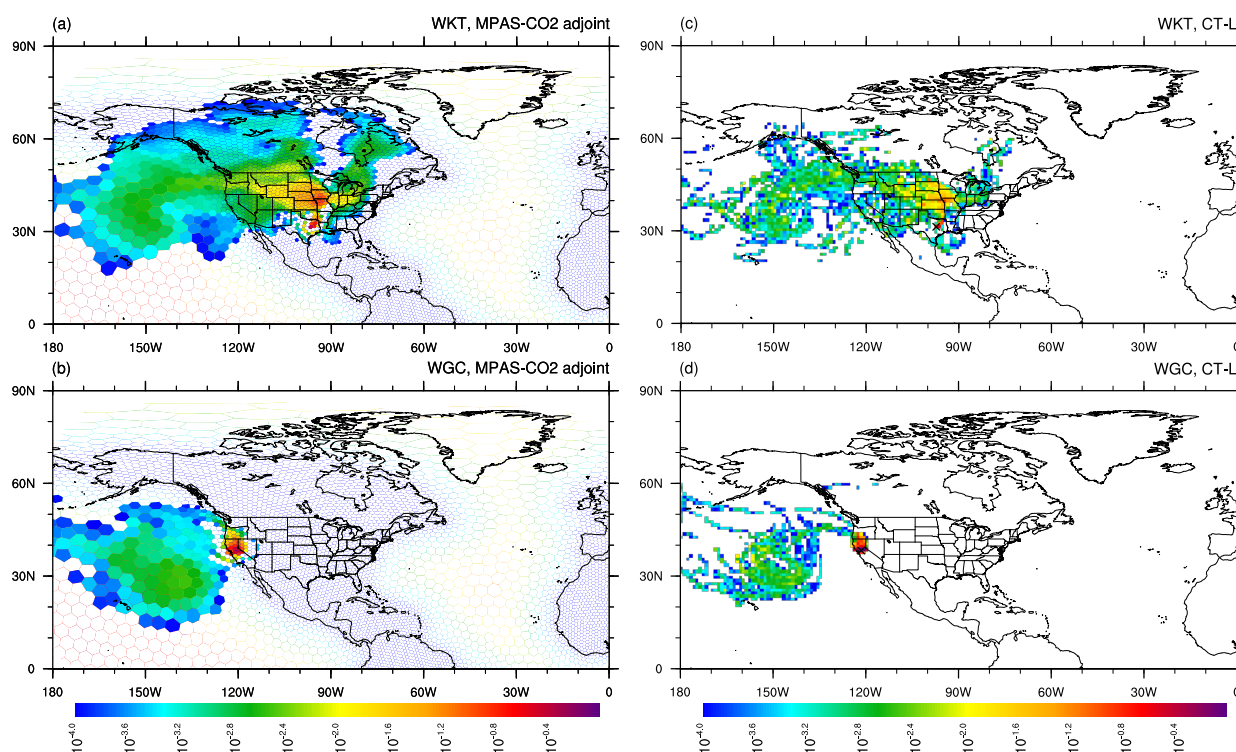


Figure 4. The 10-day backward in time CO_2 measurement footprint (units: $\text{ppm}/\mu\text{mol m}^{-2} \text{s}^{-1}$) given by two tall towers: WKT and WGC. The figures on the top panel are the footprint of the WKT tower calculated using the MPAS- CO_2 adjoint model (a) and CT-L (c). The figures on the bottom panel are the footprint of the WGC tower calculated by the MPAS- CO_2 adjoint model (b) and CT-L (d). The location of the towers is marked by the black crosses in the figure on the right panel.

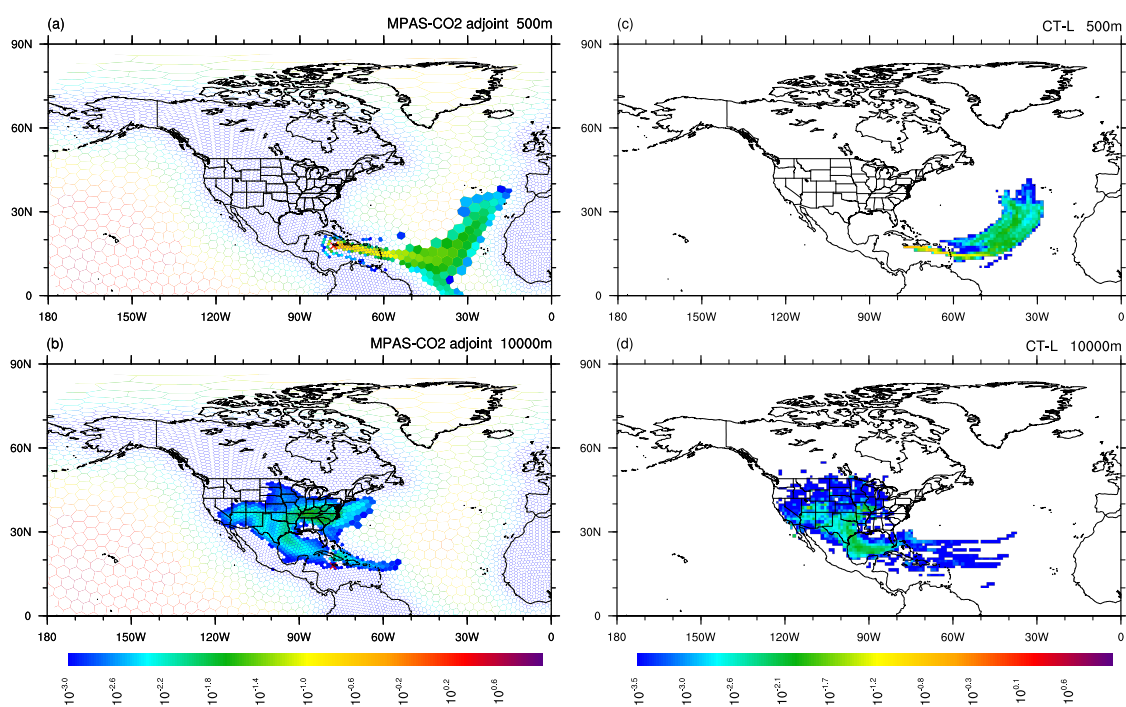


Figure 5. Comparison of footprints calculated by MPAS-CO₂ adjoint model and CT-L at a sounding location (red crosses, left panels) along the OCO-2 ground track in Fig 1 (blue color). The footprints are calculated at two different heights: 500m (top panel) and 10,000m (bottom panel), and 10 days backward in time.

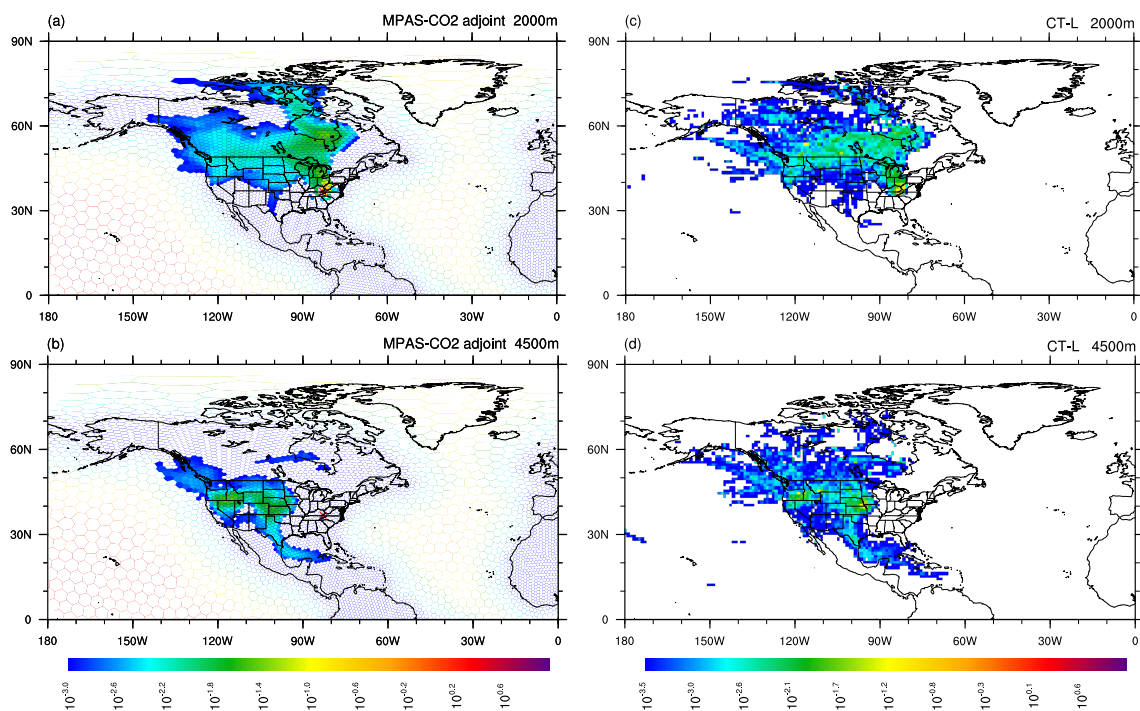


Figure 6. Same as Figure 5, except for a different OCO-2 sounding location and heights (2,000m in the top panel and 4,500m in the bottom panel).

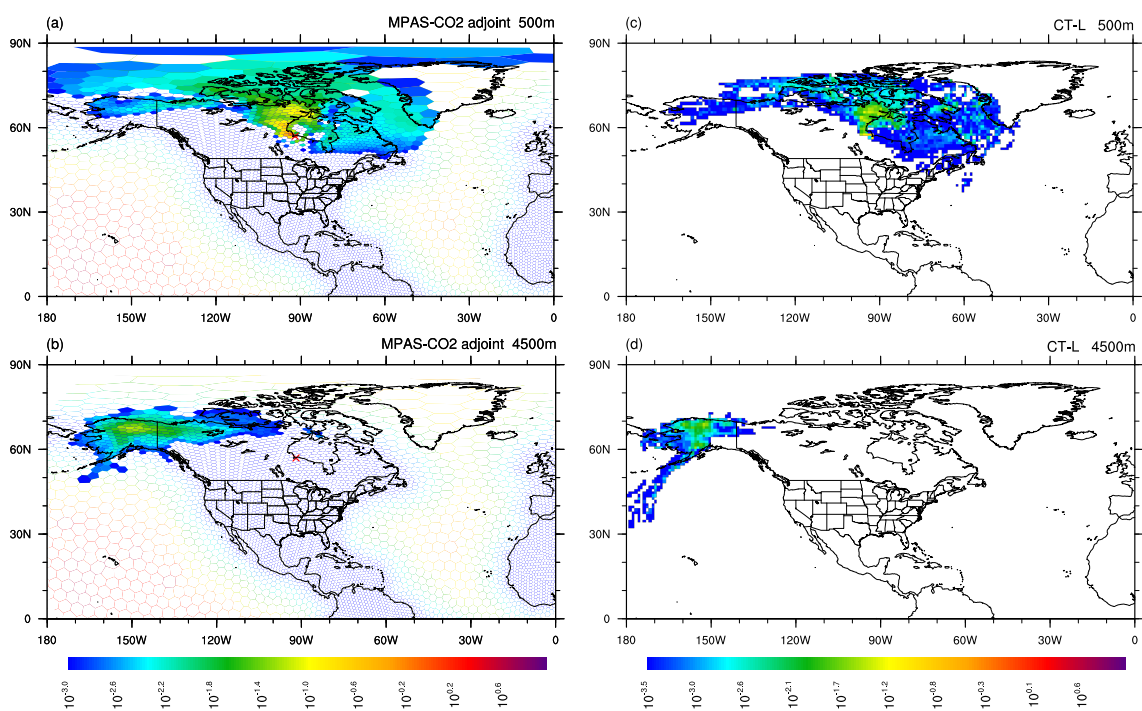


Figure 7. Same as Figure 5, except for a different OCO-2 sounding location and heights (500m in the top panel and 4,500m in the bottom panel).

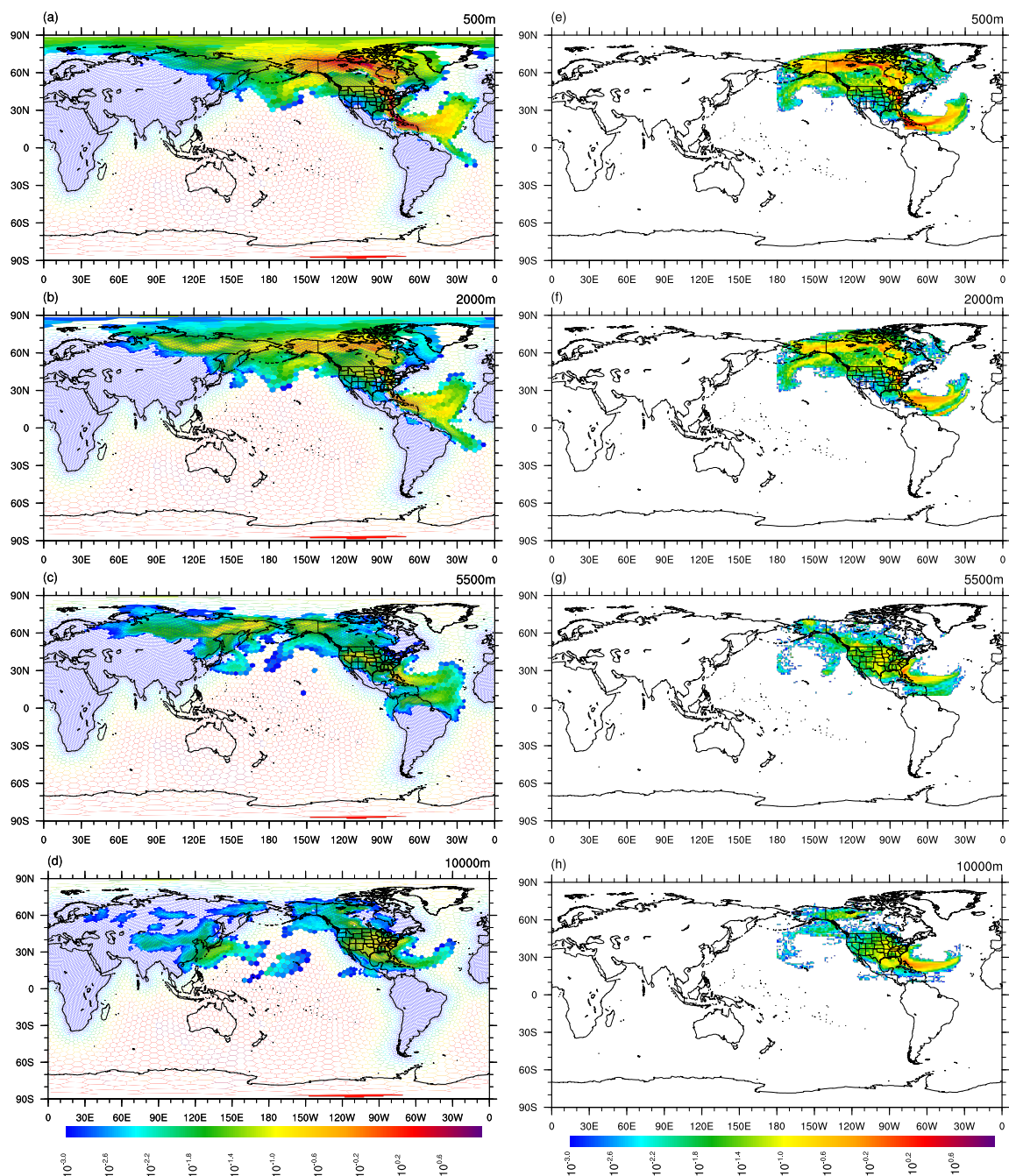


Figure 8. The footprint of the OCO-2 ground track shown in Fig. 1 (with blue color) calculated by the MPAS-CO₂ adjoint model (left panel) and by CT-L (right panel). The footprints are calculated by placing the adjoint forcing (for the MPAS-CO₂ adjoint model) or releasing particles (for CT-L) at four different height levels above the ground: 500m, 2000m, 5500m, and 10000m. The footprints are computed for 10 days backward in time.

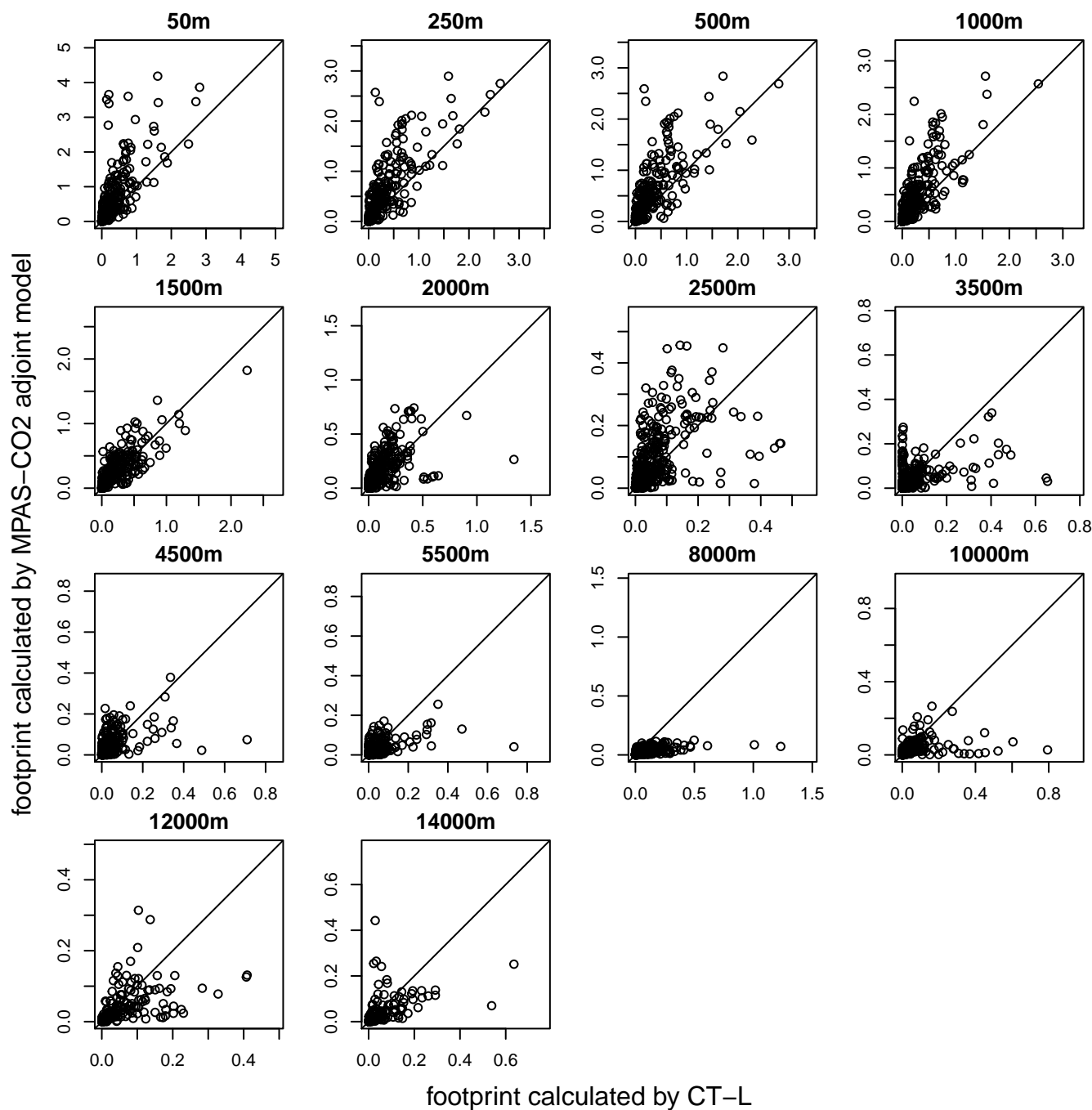


Figure 9. Comparison of the OCO-2 groundtrack footprints from the MPAS-CO₂ adjoint model and CT-L after 10 days integration backward-in-time. For each of 14 height levels, the values of the footprints (units: ppm/μmol m⁻² s⁻¹) are extracted as the average value of 2°x3° boxes within the range of the CT-L spatial domain (10-80°N, 180-10°W).

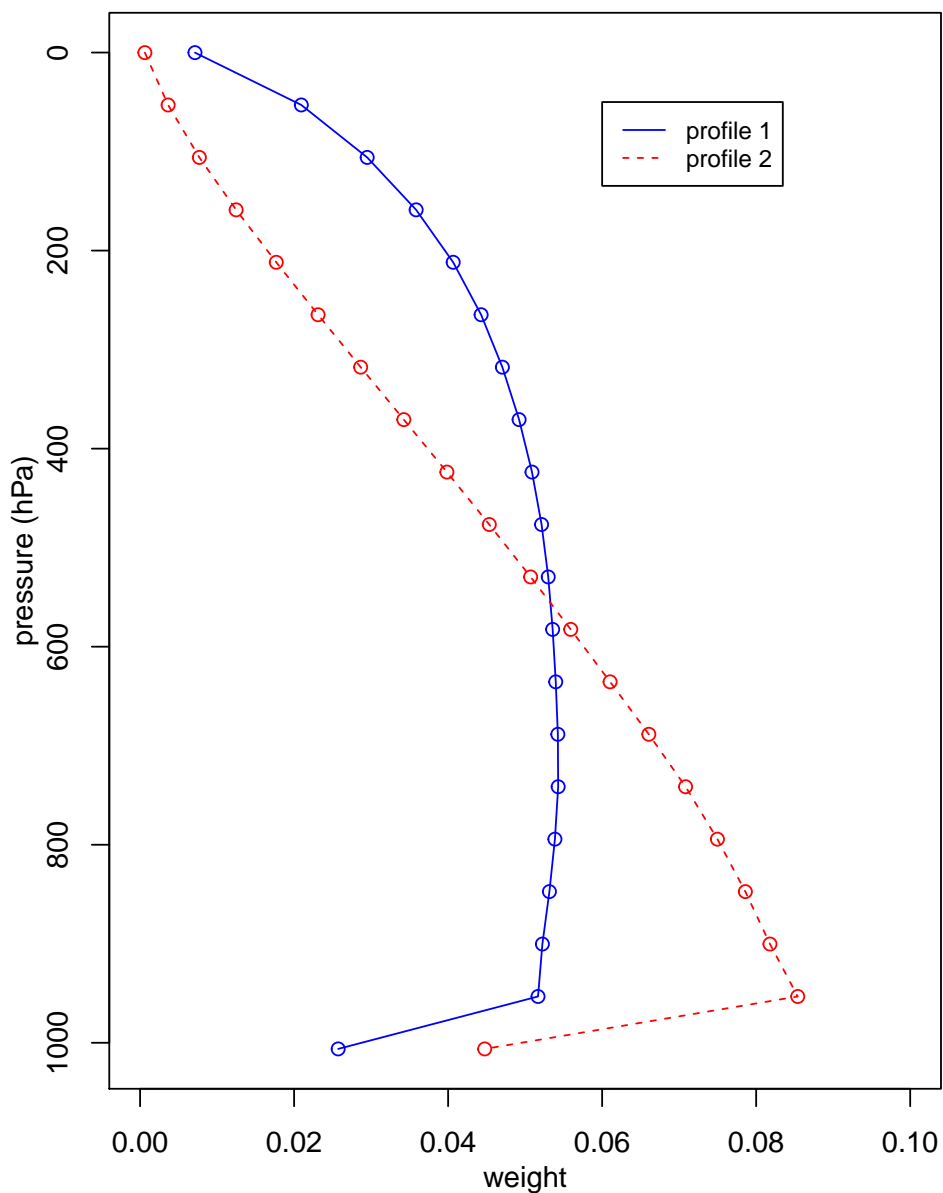


Figure 10. Two different profiles for vertically distributing a unit (ppm) of X_{CO_2} . Profile 1 is determined by OCO-2 X_{CO_2} averaging kernel and pressure weight functions. Profile 2 is based on a redistribution of Profile 1 that gives more weight towards CO_2 in the lower troposphere than in the upper part of the atmospheric column. The circles of profiles are on the twenty pressure levels of OCO-2 X_{CO_2} pressure weight function. Both profiles integrate to unity.

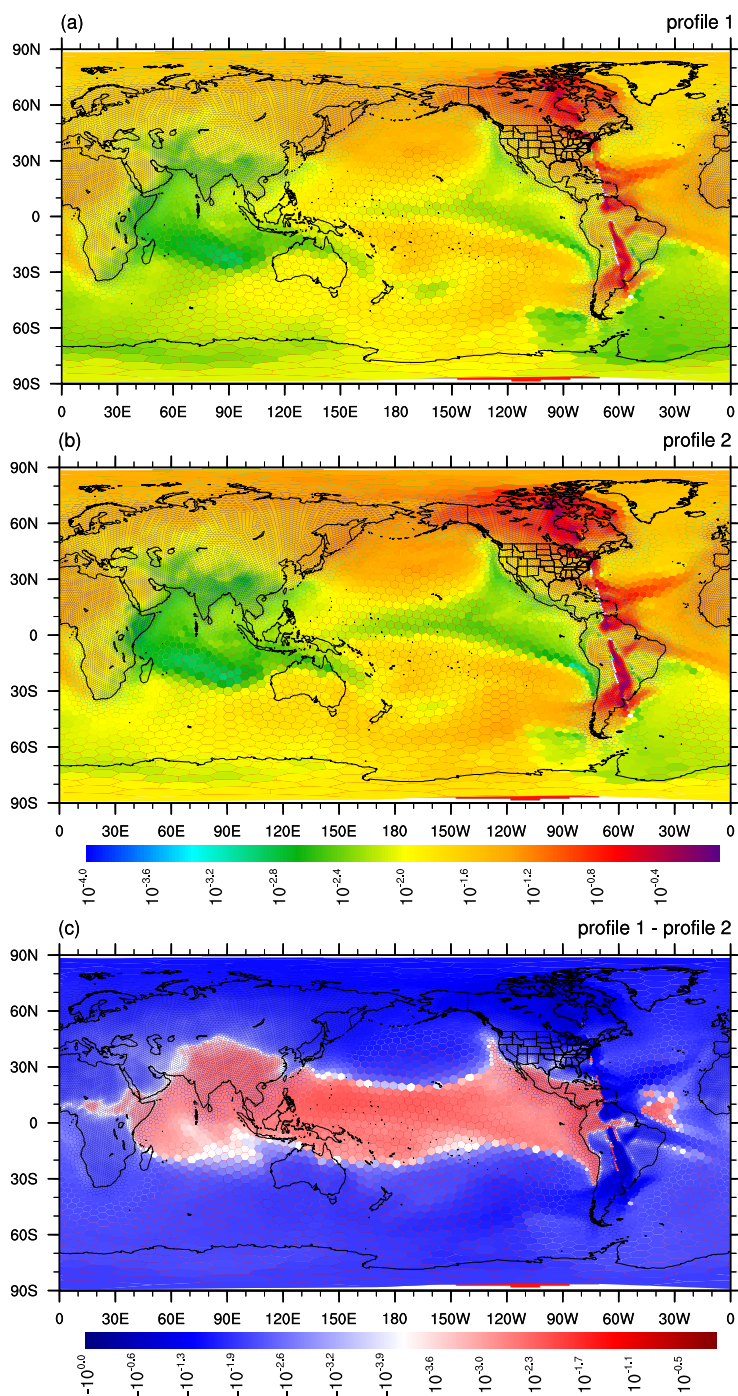


Figure 11. MPAS-CO₂ adjoint model-calculated footprints (units:ppm/ $\mu\text{mol m}^{-2} \text{s}^{-1}$) obtained after 30 days of backward-in-time integration starting on August 23, 2016 at 18:00 UTC (the time of the OCO-2 measurement). The top figure is obtained when using Profile 1 (Fig. 10) to vertically distribute 1 ppm of adjoint forcing. The middle figure is the footprint using Profile 2. The bottom figure is the difference in footprint between the two profiles.



Table 1. Results of the correctness check for the newly-developed MPAS-CO₂ tangent linear model. The results are from 1-month integration (from 2018-10-01 00:00 UTC to 2018-11-01 00:00 UTC) of the forward and tangent linear models using the 120-480 km global variable-resolution mesh (Fig. 1). The terms in the table refer to Eq. (9).

α	$\ \mathcal{M}(\mathbf{x}_0, (1 + \alpha)\mathbf{k}) - \mathcal{M}(\mathbf{x}_0, \mathbf{k}) \ $	$\ \mathbf{M}(0, \alpha\mathbf{k}) \ $	$\ \mathcal{M}(\mathbf{x}_0, (1 + \alpha)\mathbf{k}) - \mathcal{M}(\mathbf{x}_0, \mathbf{k}) \ / \ \mathbf{M}(0, \alpha\mathbf{k}) \ $
1.0×10^3	$2.07316571683768 \times 10^1$	$2.07316571683768 \times 10^1$	1.0
1.0×10^2	$2.07316571683768 \times 10^{-1}$	$2.07316571683768 \times 10^{-1}$	1.0
1.0×10^1	$2.07316571683768 \times 10^{-3}$	$2.07316571683768 \times 10^{-3}$	1.0
1.0	$2.07316571683769 \times 10^{-5}$	$2.07316571683768 \times 10^{-5}$	1.0
1.0×10^{-1}	$2.07316571683765 \times 10^{-7}$	$2.07316571683768 \times 10^{-7}$	0.999999999999998
1.0×10^{-2}	$2.07316571683799 \times 10^{-9}$	$2.07316571683768 \times 10^{-9}$	1.000000000000015
1.0×10^{-3}	$2.07316571683735 \times 10^{-11}$	$2.07316571683768 \times 10^{-11}$	0.999999999999984
1.0×10^{-4}	$2.07316571692815 \times 10^{-13}$	$2.07316571683768 \times 10^{-13}$	1.00000000004364



Table 2. Results of the correctness check for the newly-developed adjoint model of MPAS-CO₂. All simulations are of the 120-480km variable-resolution mesh (Fig. 1). The LHS and RHS in the table refer to Eq. (11).

Integration length	LHS		RHS	(LHS-RHS)/LHS
	$\Delta \mathbf{k} = 10^{-1} \mathbf{1}$ and $\Delta \mathbf{x} = \mathbf{M}(0, \Delta \mathbf{k})$			
7-day	$1.436630106778291 \times 10^{-7}$	$1.436630106778298 \times 10^{-7}$		$-5.158974640379662 \times 10^{-15}$
31-day	$2.073165716837682 \times 10^{-7}$	$2.073165716837683 \times 10^{-7}$		$-2.553561385538706 \times 10^{-16}$
	$\Delta \mathbf{k} = 10^{-1} \mathbf{1}$ and $\Delta \mathbf{x} = \mathcal{M}_{14d}(\mathbf{x}_0, \mathbf{1})$			
7-day	$2.273936055720336 \times 10^{-5}$	$2.273936055720344 \times 10^{-5}$		$-3.421966688503031 \times 10^{-15}$
31-day	$7.640482494092126 \times 10^{-5}$	$7.640482494092106 \times 10^{-5}$		$2.660668452525361 \times 10^{-15}$



Table 3. The computational costs for a 30-day simulation of MPAS-CO₂ at ~120km quasi-uniform resolution and at a variable resolution ranging from ~120 km to ~480 km. Computational costs are shown for the forward, tangent linear, and adjoint models. All simulations are conducted using 128 AMD EPYC 7H12 2.595 GHz processors running in parallel.

Model	Resolution (km)	Cost (min)	Time step (second)
Forward	120	45	720
	120-480	20	720
Tangent linear	120	48	720
	120-480	22	720
Adjoint	120	48	720
	120-480	22	720